

Valley polarization of Landau levels driven by residual strain in the ZrSiS surface band

Christopher J. Butler,^{1,*} Masayuki Murase,² Shunki Sawada,² Ming-Chun Jiang,^{1,3} Daisuke Hashizume,¹ Guang-Yu Guo,^{3,4} Ryotaro Arita,^{1,5} Tetsuo Hanaguri,^{1,†} and Takao Sasagawa^{2,6}

¹*RIKEN Center for Emergent Matter Science, 2-1 Hirosawa, Wako, Saitama 351-0198, Japan*

²*Laboratory for Materials and Structures, Tokyo Institute of Technology, Kanagawa 226-8501, Japan*

³*Department of Physics and Center for Theoretical Physics,
National Taiwan University, Taipei 10617, Taiwan*

⁴*Physics Division, National Center for Theoretical Sciences, Taipei 10617, Taiwan*

⁵*Department of Physics, University of Tokyo, 7-3-1 Hongo Bunkyo-ku, Tokyo 113-0033, Japan*

⁶*Research Center for Autonomous Systems Materialogy,
Tokyo Institute of Technology, Kanagawa 226-8501, Japan*

In a multi-valley electronic band structure, lifting of the valley degeneracy is associated with rotational symmetry breaking in the electronic fluid, and may emerge through spontaneous symmetry breaking order, or through a large response to a small external perturbation such as strain. In this work we use scanning tunneling microscopy to investigate an unexpected rotational symmetry breaking in Landau levels formed in the unusual floating surface band of ZrSiS. We visualize a ubiquitous splitting of Landau levels into valley-polarized sub-levels. We demonstrate methods to measure valley-selective Landau level spectroscopy, to infer unknown Landau level indices, and to precisely measure each valley's Berry phase in a way that is agnostic to the band structure and topology of the system. These techniques allow us to obtain each valley's dispersion curve and infer a rigid valley-dependent contribution to the band energies. Ruling out spontaneous symmetry breaking by establishing the sample-dependence of this valley splitting, we explain the effect in terms of residual strain. A quantitative estimate indicates that uniaxial strain can be measured to a precision of $< 0.025\%$. The extreme valley-polarization of the Landau levels results from as little as $\sim 0.1\%$ strain, and this suggests avenues for manipulation using deliberate strain engineering.

I. INTRODUCTION

Numerous interesting quantum phases and phenomena are associated with the breaking of one or more crystal symmetries by the electronic fluid [1, 2]. This can apply to the breaking of rotational symmetry, which can be more dramatic in materials whose ground state hosts multiple energy-degenerate band extrema separated by a large crystal momentum. These extrema are referred to as valleys, and a broken-symmetry state allowed by the lifting of the degeneracy is said to be valley-polarized.

An instability towards a rotational symmetry breaking state may result spontaneously from many-body correlations, and examples of the resulting states include recently discovered nematic [3–6] and smectic [7–9] electronic liquid crystals. Many-body correlations can be promoted in intrinsic flatband systems or within Landau levels (LLs) [5, 10, 11]. Valley-polarized LLs can host further unusual phenomena such as intrinsic in-plane electric polarization [12, 13].

Lifting of the valley degeneracy does not necessarily require many-body correlations however, and can also be caused by external perturbations to the single-particle band structure, such as strain [5, 14]. This can lead to ambiguity in the mechanism underlying an observed symmetry breaking state. In the very recent example of a kagomé lattice superconductor, rotational symme-

try breaking that might be attributable to flatband correlations has appeared in some measurements, including scanning tunneling microscopy (STM) measurements [15, 16], but has been absent in others [17, 18], and notably is absent when deliberate steps are taken to eliminate strain [19]. Although residual strain is a ubiquitous feature of STM measurements, there has been very little study of its typical scale and potential impact, which may be especially relevant for measurements of narrow spectroscopic features of current and future interest such as flatbands and Landau levels. A more in-depth understanding of it will aid efforts to investigate and properly characterize observed symmetry breaking electronic states, and may also help to guide the exploitation of strain to achieve new functionality [20, 21].

Here we investigate ZrSiS, a material chiefly known for its Dirac nodal-line band structure [22]. We focus on its unusual ‘floating’ surface band. As first described by Topp *et al.* [23], while non-symmorphic symmetry enforces a band degeneracy at the bulk Brillouin zone boundary, this symmetry breaks down at the surface. The degeneracy is lifted and a surface band is then allowed to split off, and this creates a highly two-dimensional and fairly simple multi-valley system atop the bulk nodal-line semimetal.

Using high-resolution tunneling spectroscopy under high magnetic fields, we show that the LLs formed within the surface band generally exhibit a splitting into pairs of sub-levels. Imaging of the quasiparticle interference patterns in each sub-level shows that they are strongly valley-polarized, and allows direct r - and q -space visu-

* christopher.butler@riken.jp

† hanaguri@riken.jp

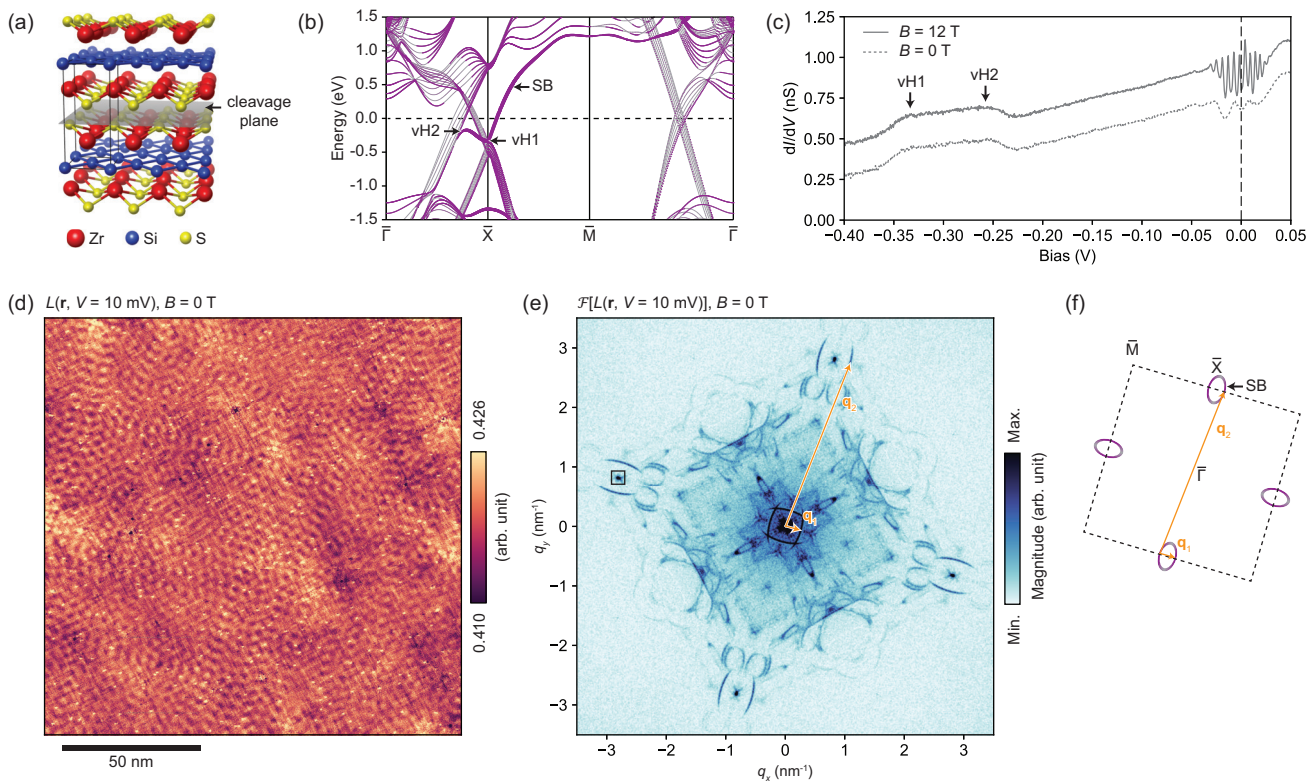


FIG. 1. Overview of the ZrSiS surface band as seen using STM. (a) Structure of ZrSiS showing a cleavage plane in gray, depicted using VESTA [24]. (b) Calculated surface band structure, with the surface projection of bulk bands in gray, and surface bands in purple. The relative size of the markers represents the relative weight of the wavefunction projected to the surface. The floating surface band is indicated (SB), as well as two nearly-flat parts of the surface band that result in van Hove-like features (vH1 and vH2). (c) Tunneling conductance $[\frac{dI}{dV}(V)]$ curves acquired under a magnetic field of $B = 12$ T and at zero field, showing the emergence of LLs near E_F ($V = 50$ mV, $I_{\text{set}} = 50$ pA, $V_{\text{mod.}} = 0.5$ mV). The curve for 12 T is vertically offset by 0.2 nS. The features vH1 and vH2 are marked, corresponding to those in (b). (d) Normalized conductance $L(\mathbf{r}, V = 10$ mV) acquired in a 150×150 nm² field-of-view ($V = 50$ mV, $I_{\text{set}} = 500$ pA, $V_{\text{mod.}} = 5$ mV), showing modulations due to quasiparticle interference. (e) Fourier transform of the image in (d), symmetrized according to the expected C_{4v} surface symmetry. A reciprocal lattice peak is marked with a black square. Two quasiparticle scattering vectors associated with the surface band are marked as \mathbf{q}_1 and \mathbf{q}_2 . (f) Depiction of the iso-energetic contour of the surface band near E_F (the bulk bands are neglected). The origins of \mathbf{q}_1 and \mathbf{q}_2 in scattering within and between surface band pockets, respectively, are shown.

alizations of the orientation of the valley-split system. We demonstrate a method for obtaining valley-selective $\frac{dI}{dV}(V)$ spectra that has broad applicability to multi-valley systems. We also introduce a model-free method for inferring the indices of observed LLs even where the lowest LL cannot be seen, and this method has the added outcome of a direct measurement of the Berry phase around the LL orbit. These methods allow us to separately and precisely describe the dispersion for each valley of the surface bands. Comparison of the dispersion curves for different pairs of valleys indicates a rigid valley-dependent contribution to the band energies.

The observation of sample dependence of the valley splitting, as well as a case of zero splitting, rules out spontaneous symmetry breaking order. Instead, we attribute the observations to residual strain. With the help of *ab initio* band structure calculations we derive a quantitative estimate for the uniaxial strain that would cause the observed valley splitting. This is also an estimate

of the typical residual strain that should be expected in a generic STM measurement prepared in a similar way. This work shows that even a small strain on the order of $\sim 0.1\%$ can lead to a dramatic rotational symmetry breaking in an energetically narrow electronic state, and in principle that this strongly symmetry breaking state can be manipulated by even weak perturbations.

II. RESULTS

A. STM observations of the ZrSiS surface band and Landau quantization

Figure 1 gives an overview of the ZrSiS surface band and some of its manifestations as seen in STM measurements. The crystal structure of ZrSiS is shown in Fig. 1(a), with the cleavage plane depicted in gray. The structure belongs to the space group $P4/nmm$ and cleavage

results in (001) surfaces with C_{4v} symmetry. Usually these surfaces are terminated by S atoms, but S contributes very little to the density of states near E_F , so atomic corrugations in STM images typically correspond to the uppermost Zr layer [25]. (A Si-terminated surface has also been reported [26], but was not observed in this work.)

Figure 1(b) shows the band structure calculated for the S-termination using the density functional theory (DFT) framework, with the surface band shown in purple. Proceeding from the \bar{X} point along the $\bar{X}\bar{M}$ line at the Brillouin zone boundary the floating surface band starts from around -300 meV and rises linearly to cross E_F . Here it is isolated by a large energy interval from any bulk counterpart. In angle-resolved photoemission measurements it can be seen as a ‘v’ shape along a $\bar{M}\bar{X}\bar{M}$ cut, and in Fermi surface imaging it is shown to cross E_F on a small elliptical loop enclosing the \bar{X} point, giving the impression its shape is similar to a cone [27]. Its behavior along the $\bar{\Gamma}\bar{X}$ line is somewhat more complicated however, having one branch that starts off flat from \bar{X} and rises slightly before turning downward to merge with the bulk nodal-loop. The partially flat bottom of the band and the downward turn are each thought to contribute a van Hove-like peak in the density of states [28, 29]. These are marked as vH1 and vH2 in Fig. 1(b). Like the lower branch, the $\bar{\Gamma}$ -facing side of the cone also mixes with bulk states.

Figure 1(c) shows high energy resolution $\frac{dI}{dV}(V)$ curves acquired at $T = 1.5$ K at a cleaved ZrSiS surface. The features corresponding to vH1 and vH2 are marked, and the energy of vH1, about 330 mV below E_F , can be interpreted as the energy of the band bottom. A comparison of the curves acquired under a magnetic field of $B = 12$ T perpendicular to the surface (solid curve), and at zero field (dashed), shows the emergence of LLs near E_F . These LLs will be shown below to occur within the surface band.

Spectroscopic-imaging STM measurements can be used to image quasiparticle interference patterns resulting from scattering at defects, from which we can infer limited information about momentum-space structures. For this we measure the tunneling conductance $\frac{dI}{dV}(\mathbf{r}, V)$ over a 150×150 nm² field of view, first under zero magnetic field. To mitigate artifacts caused by tip-height variations we then compute the normalized conductance, $L(\mathbf{r}, V) = [\frac{dI}{dV}(\mathbf{r}, V)]/[I(\mathbf{r}, V)/V]$, a quantity that is approximately proportional to the local density of states [30]. Figure 1(d) shows a representative image extracted at $V = 10$ mV. The prominent modulations are standing waves resulting from quasiparticle interference.

Figure 1(e) displays the Fourier transform $\mathcal{F}[L(\mathbf{r}, V = 10 \text{ mV})]$, which includes information about the momentum transfer vectors \mathbf{q} that are allowed upon scattering of quasiparticles. Because the atomic lattice is also resolved, reciprocal lattice peaks appear as sharp spots, one of which is marked with a black square. The scattering signals that appear as sets of ‘brackets’

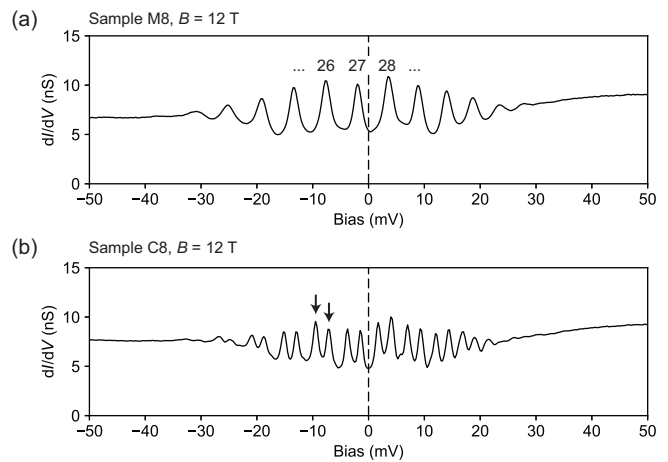


FIG. 2. Observation of Landau levels. (a) A $\frac{dI}{dV}(V)$ curve acquired at the ZrSiS surface (sample M8, $V = 50$ mV, $I_{\text{set}} = 500$ pA, $V_{\text{mod.}} = 0.25$ V). The index n for a few of the LLs is indicated. (b) A similar $\frac{dI}{dV}(V)$ curve acquired on another sample (C8) showing an apparent doubling of the number of LL peaks. Two peaks that appear to be sub-levels originating from the same level in (a) are marked with black arrows.

around each reciprocal lattice peak are the result of scattering of quasiparticles from one surface band pocket to another on the opposite side of the Brillouin zone, as illustrated in Fig. 1(f) [25, 26, 29, 31]. Scattering within each of the surface band pockets manifests as similar sets of brackets around $q = 0$, but here the scattering signals originate from pockets in both orientations, and overlap to give the appearance of a square. (To our knowledge, scattering between one surface band pocket and one of its 90° rotated partners has not been reported.) All other scattering signals appearing in Fig. 1(e) are the result of scattering within the bulk nodal-loop, or between the nodal-loop and the surface bands. Some of these features have been understood in previous analyses [25, 26, 29, 31–33] and will not be considered further here. There also exist features that have not been described previously, which appear only at low energies, and which will be the subject of a future report. For the following discussion we only note that the ‘bracket’ signals serve as the hallmark of the surface band in quasiparticle interference observations, and the signals from sets of valleys related by a 90° rotation are easily distinguishable.

Focusing again on the LLs, Fig. 2(a) shows a measurement of $\frac{dI}{dV}(V)$ averaged over a 4×4 nm² field of view (sample M8 - sample naming is explained in Supplementary Note 1). We first note that LLs appear only in an energy interval very near to E_F . This is very similar to the appearance of LLs previously reported in the surface band of the sister compound HfSiS [34]. Some attenuation of LL peak intensity away from E_F is a nearly universal feature of LL spectroscopy measurements performed using STM [5, 34–38]. (One of the possible explanations is the effect of electron-phonon interactions, and in the

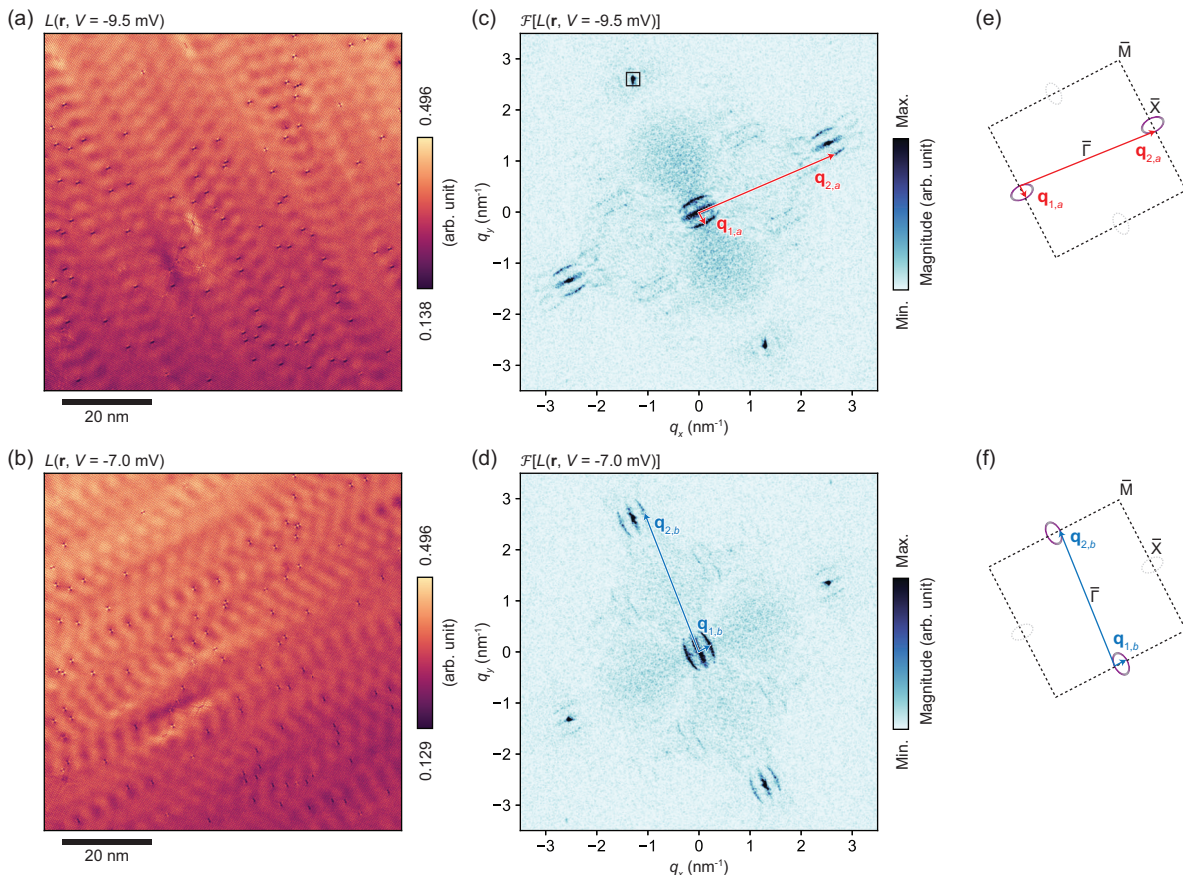


FIG. 3. Imaging quasiparticle interference within valley-polarized LLs. (a) and (b) Normalized conductance images measured in the same $80 \times 80 \text{ nm}^2$ field-of-view, under $B = 12 \text{ T}$ ($V = 50 \text{ mV}$, $I_{\text{set}} = 500 \text{ pA}$, $V_{\text{mod.}} = 0.3 \text{ mV}$). The energies correspond to those of the pair of LL peaks marked with black arrows in Fig. 2(b). (c) and (d) The corresponding Fourier transform images. Prominent ‘bracket’ scattering signals enclose only one set of reciprocal lattice peaks at each energy, and the patterns of scattering appear to be related by a 90° rotation. The box-like signal around $q = 0$ is also broken into the bracket-like subsets indicating intra-pocket scattering. (e) and (f) The origins of $\mathbf{q}_{1,a(b)}$ and $\mathbf{q}_{2,a(b)}$ in scattering within and between surface band pockets.

present case LL peaks abruptly disappear upon reaching the energy of a particular phonon mode, namely a previously described E_g mode with an energy of about 18 meV [39].) Due to this effect, LLs may be formed in a band that spans a large energy range while only being measurable in a very narrow range. Generally the lowest LL may not then be observed and the indices of the observable LLs are not immediately known [we label them in Fig. 2(a) with the benefit of advance knowledge of the following results]. We discuss this problem and introduce a generally applicable and robust solution to it in Section D.

Figure 2(b) shows another $\frac{dI}{dV}(V)$ curve that was acquired under the same experimental conditions as the one shown in (a), but on a different sample (C8). This curve exhibits an apparent doubling of the number of LL peaks as compared to the measurement in (a). A reasonable guess is that there is a splitting of each LL feature into a pair. One such pair is marked in Fig. 2(b) by black arrows.

B. Imaging valley-polarized LLs

In Fig. 3(a) and (b) we show images extracted from a $L(\mathbf{r}, V)$ measurement at the energy of each of the peaks in the pair marked in Fig. 2(b), specifically at $V = -9.0 \text{ mV}$ and $V = -7.5 \text{ mV}$, respectively. In each case the field-of-view is covered by highly coherent uniaxial modulations of the local density of states, that change orientation by 90° from one LL feature to the other. This difference is clarified in the corresponding Fourier transform images $\mathcal{F}[L(\mathbf{r}, V)]$ shown in Figs. 3(c) and (d). Aside from the reciprocal lattice peaks, the most prominent features are the ‘bracket’ signals characteristic of scattering between surface band pockets, and the signals due to scattering in the bulk bands are almost completely absent. First and foremost, this confirms that the observed LLs form in the surface band. At each energy, the inter-pocket scattering between only one pair of surface band pockets (\mathbf{q}_2) appears, and the intra-pocket scattering (\mathbf{q}_1) only within the pockets of that pair appears near $q = 0$. This shows

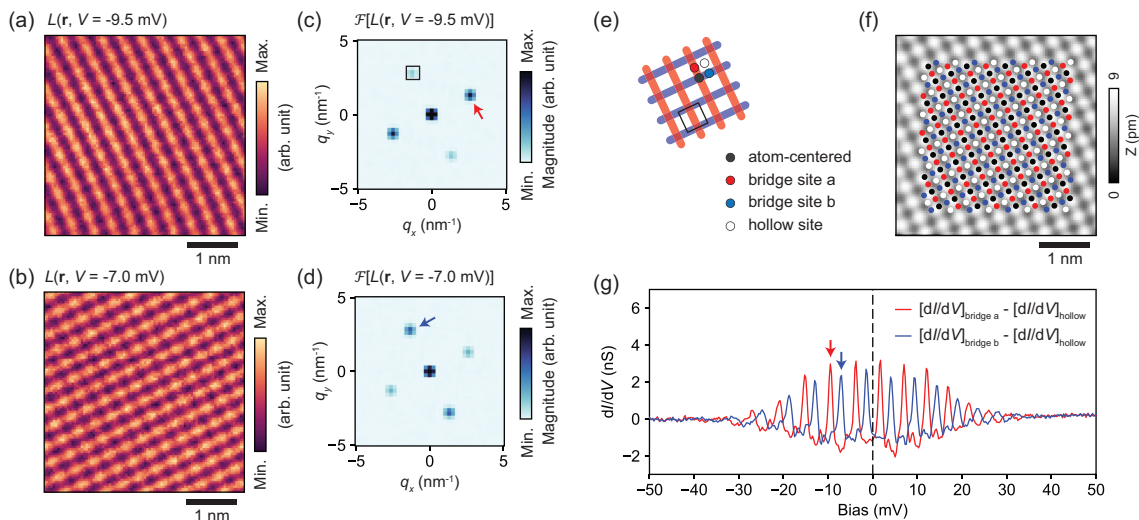


FIG. 4. Obtaining valley-specific LL spectra using intra-unit-cell sampling of density of states. (a) and (b) Normalized conductance images acquired in a $4 \times 4 \text{ nm}^2$ field-of-view. The energies are those of the two LLs resolved in Fig. 3, and marked with black arrows in Fig. 2(b). A subtle difference can be seen in the intensity of lattice-commensurate stripes, with a 90° relative rotation between the two images. (c) and (d) The corresponding Fourier transform images. The difference manifests as the differing intensity around the reciprocal lattice points [one of which is marked with a black square in (c)]. The small r -space field-of-view results in a low q -space resolution, meaning that the Fourier transforms in (c) and (d) are effectively course-grained versions of those in Fig. 3(c) and 3(d) above. The quasiparticle scattering signals are now indistinguishable from the reciprocal lattice peaks, and their inverse Fourier transforms generate lattice-commensurate stripes. (e) An illustration of the resulting striped patterns, with one unit cell of the Zr square net marked in black. The sub-lattice sampling sites are marked with dots. (f) The sub-lattice sampling grids generated for this field of view (see Supplementary Note 3), shown on top of the simultaneously acquired topography image. (g) The valley-specific contributions to the conductance are obtained by subtracting the hollow site background from the bridge site curves.

that the splitting apparent in the $\frac{dI}{dV}(V)$ curve shown in Fig. 2(b) is associated with the valley degree of freedom. We now make a distinction between scattering between each of the two sets of pockets by labeling them with scattering vectors $\mathbf{q}_{1,a}$ and $\mathbf{q}_{2,a}$ within one set, and $\mathbf{q}_{1,b}$ and $\mathbf{q}_{2,b}$ within the other (in relation to the \mathbf{a}_0 and \mathbf{b}_0 lattice vectors). The origins of the scattering patterns shown in (c) and (d) are illustrated in (e) and (f), respectively. Surprisingly, scattering within the bulk bands appears to be absent at the low energies ($|eV| < 10 \text{ meV}$) where LLs are imaged, so that the L and $\mathcal{F}[L]$ images extracted between LLs are almost featureless (see Supplementary Note 2).

C. Valley-selective LL spectroscopy

We now describe a method of measuring valley-selective density of states spectra. This technique exploits the fact that in multi-valley systems, scattering vectors between valleys on opposing sides of the Brillouin zone are close to one of the reciprocal lattice vectors, and therefore their corresponding r -space modulations are effectively commensurate with the lattice. Due to the differing orientation of modulations derived from different valleys, a careful intra-unit-cell sampling of the measured local density of states can be used to extract the valley-

specific contributions, and this can be done by measuring in only a very small field of view.

Figure 4 shows the implementation of this method for a $\frac{dI}{dV}(\mathbf{r}, V)$ measurement in a $4 \times 4 \text{ nm}^2$ field of view. Panels (a) and (b) show images of $L(\mathbf{r}, V = -9.5 \text{ mV})$ and $L(\mathbf{r}, V = -7.0 \text{ mV})$, corresponding to the energies of the LLs visualized in Fig. 3. A very subtle C_2 symmetric and commensurate stripe pattern can be seen superimposed on the modulations of the square Zr lattice. The $\mathcal{F}[L(\mathbf{r}, V)]$ images are shown in Figs. 4(c) and (d). The intensity of the signal around the reciprocal lattice peaks shows the same reduction to C_2 symmetry as seen in Figs. 3(c) and (d). In panel (e) we illustrate the two superimposed lattice-commensurate stripe patterns, which can be thought of as the inverse Fourier transforms of the peaks marked in panels (c) and (d). At the r -space points that we label as the ‘bridge a ’ and ‘bridge b ’ sites, in principle, the contribution to the local density of states from either the ‘ a ’ or ‘ b ’ valley dominates the signal. Figure 4(f) shows four sets of sampling sublattices, including the a and b bridge sites, the atom-centered (Zr-centered) sites, and the hollow sites. We average the curves over each of the four sets of sampling points in order to mitigate noise, and take the curve from the hollow sites as a baseline that we subtract from the a and b site curves. The resulting valley-specific curves are shown in (g), and these can be compared against the

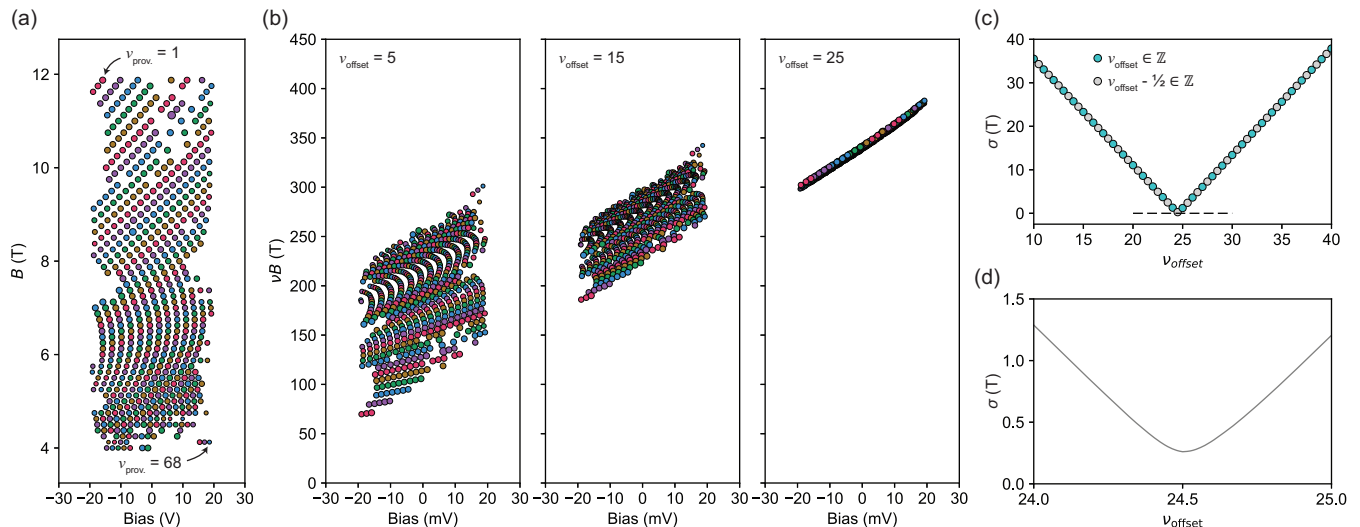


FIG. 5. Obtaining LL indices and Berry phase. (a) Energies of LLs obtained (see Supplementary Note 3) at a range of different magnetic fields, from the $\frac{dI}{dV}(V)$ curves sampled at the a sublattice sites [e.g. the red curve in Fig. 4(g)]. Points belonging to the same LL are plotted with the same color. (b) The same points shown in a plot of νB versus energy, and the resulting plot given three trial values for ν_{offset} . The arrangement of points narrows as ν_{offset} approaches ~ 25 . (c) The spread of points, σ , plotted against ν_{offset} . Gray and green markers denote values of ν_{offset} that correspond to topologically trivial and non-trivial cases, respectively. σ is minimized when $\nu_{\text{offset}} = 24.5$ (topologically trivial). (d) Under the pretense that ν_{offset} is not quantized but is instead a continuous variable, a precise value for ν_{offset} can be obtained.

spatially averaged curve shown above in Fig. 2(b).

We perform a similar procedure to obtain valley-specific LL spectra under external magnetic fields between $B = 4$ T and 12 T in increments of 125 mT. Using a further peak fitting procedure we can obtain values for the LL energies at each field value, building up comprehensive LL fan diagrams from which further band properties can be inferred. (See Supplementary Note 3 for all curves and for details of the sampling and fitting procedures.) The LL energies obtained in this way for the a site $\frac{dI}{dV}(\mathbf{r}, V)$ curves are shown in Fig. 5(a).

D. Model-free determination of LL indices and Berry phase

According to the Lifshitz-Onsager quantization condition, the extremal cross-sectional area S encompassed by the n^{th} LL orbit in k -space is expressed as

$$S_n = \frac{2\pi eB}{\hbar} \left(n + \frac{1}{2} - \frac{\gamma_B}{2\pi} \right), \quad (1)$$

where \hbar is the reduced Planck constant, e is the electron charge, n is an integer ($n \in \mathbb{Z}$), and γ_B is the Berry phase. For the procedure that follows, it is useful to define a number

$$\nu = n + \frac{1}{2} - \frac{\gamma_B}{2\pi} \quad (2)$$

which we will also refer to loosely as the LL ‘index’. If the LL orbit encloses a topologically non-trivial point in

the band structure, with $\gamma_B = \pi$, then $\nu \in \mathbb{Z}$. If not, then $\nu - \frac{1}{2} \in \mathbb{Z}$. (The surface bands of ZrSiS are thought to emerge from a topologically trivial point.)

The energy spectrum of the LLs depends on how the area S changes with energy, which depends on the details of the band dispersion. Assuming an isotropic dispersion, a circular orbit with area S_ν has a radius

$$k_\nu = \sqrt{\frac{2e\nu B}{\hbar}}. \quad (3)$$

For any dispersion relation $E(k)$, the energy of the n^{th} LL is seen to scale as $(\nu B)^\alpha$, with $\alpha = 1$ for a parabolic band, $\alpha = \frac{1}{2}$ for a Dirac-like band, and other values for other, more exotic cases [40]. Given observed energy values for LLs such as those shown in Fig. 5(a), a plot of E -versus- νB [or equivalently a νB -versus-bias plot as shown in Fig. 5(b)] causes all the points to fall on the same curve, but this requires the correct assignment of the index ν_i to the i^{th} data point. The collapse of points into a curve occurs regardless of the scaling α that encapsulates the detailed dispersion. Our approach is to search the space of possible LL index assignments for the set that yields this curve.

The first step is to assign a set of provisional indices ν_{prov} that will generally be wrong, but in such a way that any difference in index between any two data points is correct. This means that the error in assignment of indices is uniform over the whole set of data points, and also that the search space will only be one-dimensional. As shown in Fig. 5(a) we begin at the top-left-hand corner of the B -versus-bias plot, starting with $\nu_{\text{prov}} = 1$.

We proceed downwards, labeling LLs until reaching the highest observed LL at $\nu_{\text{prov.}} = 68$ for the 614th data point. In this case the error, which we call ν_{offset} , corresponds to the number of unobservable LLs at energies lower than ~ 20 meV. For the i^{th} point the true index is given by $\nu_i = \nu_{\text{prov.,}i} + \nu_{\text{offset}}$. Now plotting the points in νB -versus-bias space as in Fig. 5(b), we vary ν_{offset} and observe which value causes the plot to collapse into a narrow curve. To aid this process we define a value σ that characterizes the spread of the data points that we aim to minimize. This is obtained by sorting the data points by energy, summing the differences along the νB axis between neighboring points, and finally dividing by the total number of data points N . This is written as

$$\sigma(\nu_{\text{offset}}) = \frac{1}{N} \sum_{i=1}^{N-1} |\nu_{i+1} B_{i+1} - \nu_i B_i|. \quad (4)$$

The correct LL indices ν_i are found where the choice of ν_{offset} minimizes σ , i.e.:

$$\nu_i = \nu_{\text{prov.,}i} + \underset{\nu_{\text{offset}}}{\text{argmin}} \sigma \quad (5)$$

The number ν_{offset} also encodes the unknown Berry phase that contributes to ν (see Eq. 2) and this can take a value of zero or π so that either ν_{offset} or $\nu_{\text{offset}} - \frac{1}{2}$ is an integer. Figure 5(c) shows the variation of σ when ν_{offset} is incremented in both cases, and that it is minimized when $\nu_{\text{offset}} = 24.5$. This means that any given LL index belongs to $\mathbb{Z} + \frac{1}{2}$, the topologically trivial case. We can confirm the above result by adopting the pretense that ν_{offset} is not quantized but is instead a continuous variable as shown in Fig. 5(d). σ is minimized almost exactly at $\nu_{\text{offset}} = 24.5$. The lowest observed LL index in the data set shown in Fig. 5(a) is $n = 25$, and the highest is $n = 92$.

E. Determination of valley dispersion curves

Having assigned indices to all observed Landau levels, we have a curve in the νB -versus-bias plot that is related to the dispersion curve for the surface bands through the relation $E_\nu - E_0 \propto (\nu B)^\alpha$, where E_0 is the energy of the band bottom. Given the appearance of the surface band in the DFT calculations shown in Fig. 1(b) as well as in previous reports [23, 27], it is reasonable to adopt a linear band model with $\alpha = \frac{1}{2}$. Accordingly, Fig. 6(a) displays the surface bands modeled as a set of cones of elliptic cross-section located around the \bar{X} points of the surface Brillouin zone. Although it only partially resembles the structure shown in Fig. 1(b), it will be shown below to very accurately capture the key band properties relevant to LL formation.

Assuming linear dispersion, from Eq. 3 we have

$$E_\nu = E_0 + \tilde{v} \sqrt{2e\hbar\nu B}. \quad (6)$$

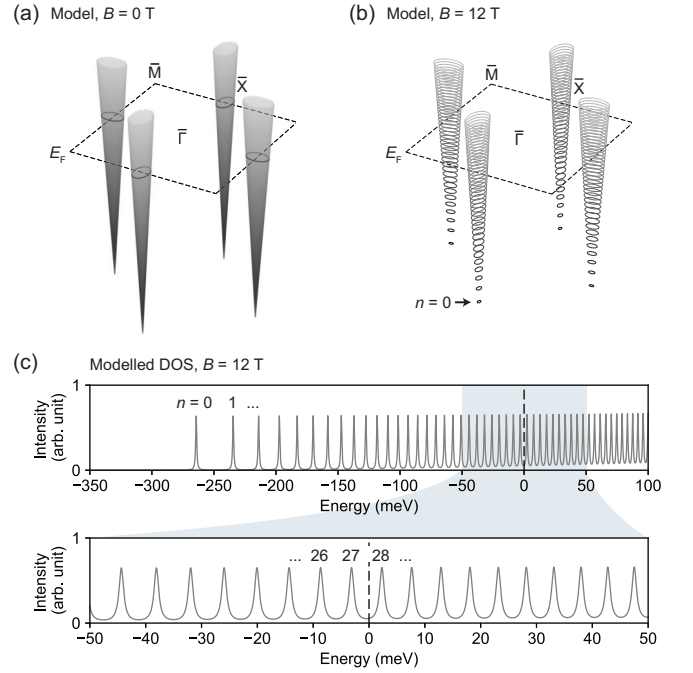


FIG. 6. Simplified model for understanding LL spectra in the surface band. (a) A model comprising a cone-shaped band at each \bar{X} point of the surface Brillouin zone. (b) A depiction of Landau quantization under a field of $B = 12$ T. (c) Modeled density of states spectrum at $B = 12$ T and a zoom-in view around E_F where LLs can be resolved in measurements. Each LL is represented as a Lorentzian lineshape.

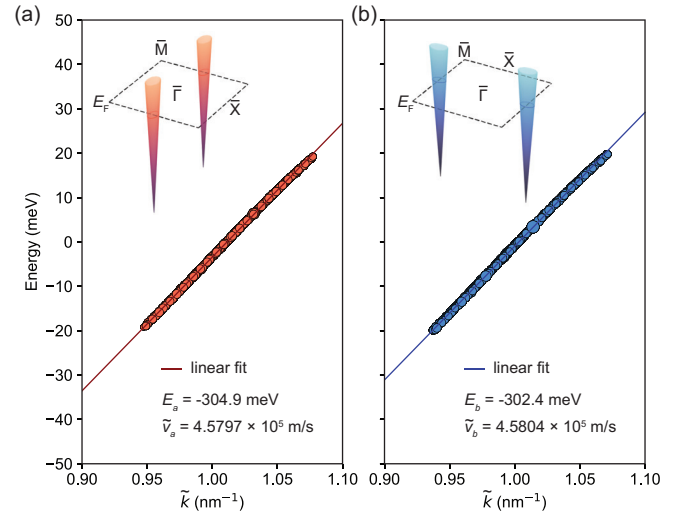


FIG. 7. Valley-selective dispersion curves of the floating surface band. (a) A dispersion curve obtained for the a valley, using LL indices with $\nu_{\text{offset}} = 24.5$ (from Fig. 5), and assuming a LL spectrum described by Eq. 6. The solid red line is a linear fit to all data points, with the resulting E_0 and average velocity \tilde{v} also shown. (b) The corresponding plot and linear fit result for the points extracted from the b sublattice site and following the same procedure as shown in Fig. 5, which also yields $\nu_{\text{offset}} = 24.5$. A comparison of the linear fitting results shows a difference $|E_b - E_a| = 2.5$ meV, and a negligible difference in band velocities.

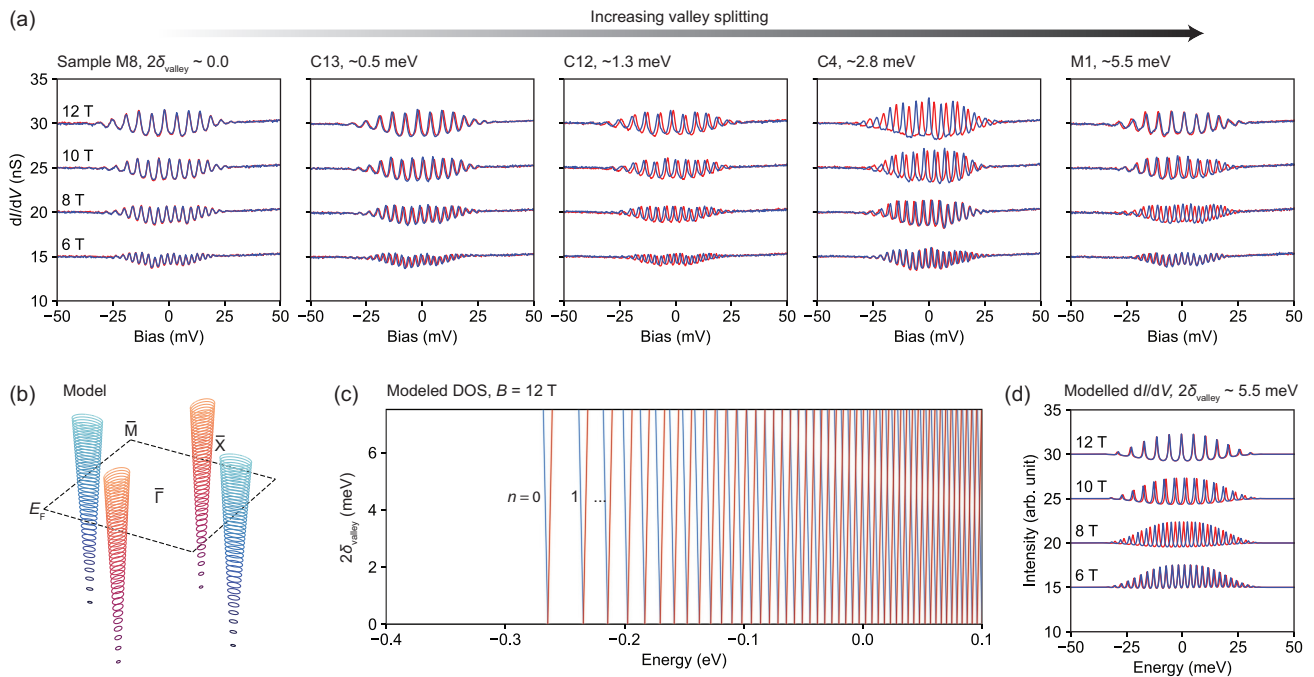


FIG. 8. Sample dependence of valley splitting. (a) Valley-selective $\frac{dI}{dV}(V)$ curves at various magnetic fields for five different samples, sorted in order of the valley splitting energy, from lowest to highest. The asymmetry seen at $B = 12$ T is greatest for sample C4. For the sample with the highest splitting, where $B \approx 12$ T the valley splitting is similar to the energy spacing between LLs. At $B = 12$ T, LLs of different filling, from different valleys, coexist at the same energy. (b) The cone model for the floating surface band. Here the two inequivalent sets of valleys are depicted in blue and red. (c) Modeled density of states for the two LL series under $B = 12$ T, plotted with varying valley splitting $2\delta_{\text{valley}}$. (d) Simulated $\frac{dI}{dV}(V)$ curves at the same magnetic fields as for (a), for a splitting of $2\delta_{\text{valley}} = 5.5$ meV. (An envelope function is applied for ease of comparison.)

Because the iso-energetic contours of the real surface bands are not circular but elliptical, we have specified \tilde{v} as the absolute band velocity on a circular orbit with the same area as the real band contour. Likewise, $\tilde{k}_\nu = \sqrt{2e\hbar\nu B/\hbar}$ is the radius in momentum space of the equivalent circular orbit. Because the LL spectrum is determined only by the area enclosed by the LL orbits, the location of the cones at the zone boundary is unimportant.

In Fig. 6(b) we illustrate the Landau quantization of the surface band cones according to Eq. 6. Figure 6(c) shows the resulting LL spectrum, as well as a zoom-in view of the energy interval of experimental interest. For these plots we adopt realistic values for E_0 and the band velocity [27], and assume the topologically trivial case, and the result very closely resembles the measured spectrum in Fig. 2(a).

We can now take the LL energies plotted in Fig. 5(a) for valley a and, using Eq. 6 with $\tilde{k}_\nu = \sqrt{2e\hbar\nu B/\hbar}$, plot the $E(k)$ curve. This is shown in Fig. 7(a). Going through a parallel process to obtain LL energies for valley b (see Supplementary Note 3), we plot the corresponding curve in Fig. 7(b). For each valley's dispersion plot we use a linear fit of the form $E = \tilde{v}_a k_a + E_a$ to estimate the energy E_a of the bottom of the band at the Brillouin zone boundary, and the velocity \tilde{v}_a around the band contours near E_F . The results of the linear fit are shown in each

panel of Fig. 7. We find that E_a and E_b differ by 2.5 meV [c.f. Figs. 3(a) and (b)], and the difference between \tilde{v}_a and \tilde{v}_b is negligible.

This information can be used to add a valley degree-of-freedom to the model described by Eq. 6. The ways of doing this could have been i) to add a rigid, valley dependent energy shift δ_{valley} , or ii) to include a valley dependent modification of the band velocity (with a third option being a combination of these effects). The results of the linear fitting show that a valley dependent difference in velocities can be safely excluded, and the total LL spectrum is then given by

$$E_{\nu,\pm} = E_0 + \tilde{v}\sqrt{2e\hbar\nu B} \pm \delta_{\text{valley}}. \quad (7)$$

Referring back to Fig. 7, we can recognize that $E_a = E_{\nu=\frac{1}{2},-}$ and $E_b = E_{\nu=\frac{1}{2},+}$.

F. Sample dependence of valley splitting

As suggested by the difference in the $\frac{dI}{dV}(V)$ curves shown in Figs. 2(a) and 2(b), there is significant sample dependence of the valley splitting. Figure 8(a) shows series of valley-selective $\frac{dI}{dV}(V)$ curves acquired from five selected samples. From left to right, the splitting is seen to increase from zero to ~ 5.5 meV.

Assuming that, in Eq. 7, E_0 and \tilde{v} have negligible sample dependence, it seems possible to simply read out the value of δ_{valley} for LL spectra observed in any sample without the process detailed in Figs. 5 and 7 above. The top row of curves in Fig. 8(a) show that this is not the case, however. If δ_{valley} is large enough, at some point it matches the LL spacing and the two curves become indistinguishable, resembling the case of $\delta_{\text{valley}} = 0$. Pairs of curves collected at more than one magnetic field are needed to unambiguously determine δ_{valley} . The values given in Fig. 8(a) are obtained by measuring a short series of curves that capture enough field dependent information, and using a trial-and-error process of simulating the corresponding field dependence for a given value of δ_{valley} .

Figure 8(b) illustrates the model underlying the LL spectra described by Eq. 7, and 8(c) shows the resulting valley dependent spectra simulated for varying δ_{valley} under $B = 12$ T. Each observation at 12 T shown in (a) corresponds to a horizontal cut through the simulation in (c). Given this, a trial-and-error search along the $2\delta_{\text{valley}}$ -axis of the simulation can be used to infer the splitting in the measured spectra, and an example of this is given in Fig. 8(d). The simulated spectra at chosen magnetic fields using $2\delta_{\text{valley}} = 5.5$ meV yields a very good match to the spectra shown in panel (a) for sample M1. The success of this procedure attests to the validity of the simple model illustrated in Fig. 8(b), that yields the LL spectrum described by Eq. 7.

III. SUMMARY AND DISCUSSION

We have used STM to observe LLs at the surface of ZrSiS under high magnetic fields. We have seen that the energies of the observed LLs closely match those of the predicted LL spectrum for the floating surface band, if it is modeled simply as a set of cones, each located at one of the \bar{X} points. But we also find that most samples exhibit an unexpected splitting of the LL spectrum. Quasiparticle interference imaging shows that the splitting manifests within the valley degree of freedom, indicating that each pair of valleys supports an independent LL spectrum related by a rigid energy difference of $2\delta_{\text{valley}}$. The valley splitting is seen to be sample-dependent, ranging from zero to a few meV.

Due to this effect, a measurement at any particular energy will generally probe a LL in at most one of the sets of valleys, as depicted in Fig. 3. We can switch between states of opposite valley-polarization by adjusting the energy by only a few meV. Also, a LL of either valley polarization can be brought to E_F using a small (~ 100 mT) adjustment of the magnetic field. In principle the valley polarization is therefore amenable to detection in a suitable quantum oscillation measurement [41]. A noteworthy complication is that a relatively large valley splitting can coincide with the energy interval between two LLs. This situation can be seen in Fig. 8(a), in

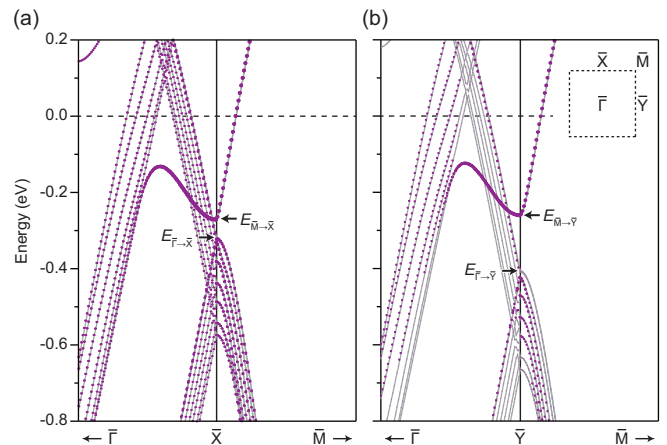


FIG. 9. Calculation of strain effects on the surface bands. (a) Surface band structure around the \bar{X} point for the case of a 1% uniaxial strain (elongating the lattice vector \mathbf{b}_0), calculated using DFT. (b) Surface band structure around the \bar{Y} point of the strained Brillouin zone (shown in the inset). There are two features in the band structure at each point that could each be identified with the bottom of one cone in the simplified model investigated above.

the 12 T measurement for sample M1, where we have the unusual case of a single spectroscopic feature composed of LLs with differing indices.

The application of a magnetic field is not thought to be responsible for the lifting of valley degeneracy and we observe no influence of magnetic field on the valley splitting. This can be verified by considering the collapse of a set of measured LL energies into a narrow curve, as shown in Fig. 5. Because this set includes points obtained under very different fields, the collapse could not occur if there was a significant field dependent contribution to the band energy. Though a lifting of the valley degeneracy under magnetic field is not expected, lifting of the two-fold spin degeneracy within each valley is expected. However, surprisingly it was not observed. The Zeeman splitting for free electrons under a field of 12 T would be ~ 1.4 meV, and no such splitting appears in either the spatially averaged or valley-resolved $\frac{dI}{dV}(V)$ curves. Even a smaller Zeeman splitting (for Landé factor $g < 2$) might be expected to cause a field-dependent contribution to the apparent width of the LL peaks, but this also was not observed (see Supplementary Note 4). The apparent absence or diminution of the Zeeman effect is noteworthy but is beyond the scope of this work.

The sample dependence of δ_{valley} , and especially the observation of $\delta_{\text{valley}} = 0$ [Fig. 8(a), sample M8] rules out any spontaneous symmetry breaking of the electronic states. Instead, the lifting of valley degeneracy is likely caused by residual strain. In Fig. 9 we show the calculated electronic band structure for 1% strained ZrSiS, focusing on the regions around the \bar{X} and \bar{Y} points of the strained Brillouin zone. At each high-symmetry point we can find two features that can be associated with the bot-

tom of the cones in our simplified model. In the real band structure, if we start from the Fermi contour around \bar{X} (or \bar{Y}), the bands extending downwards on the \bar{M} -facing and $\bar{\Gamma}$ -facing sides of the manifold reach the respective high symmetry point at different energies. In Fig. 9 we label these as $E_{\bar{M}\rightarrow\bar{X}(\bar{Y})}$ and $E_{\bar{\Gamma}\rightarrow\bar{X}(\bar{Y})}$, respectively. The former of these two features is 9.8 meV higher at \bar{Y} than at \bar{X} , while the latter is 87.3 meV lower at \bar{Y} than at \bar{X} . If we take the average of these shifts in order to draw an estimate of the corresponding valley splitting in our conical model, this gives $2\delta_{\text{valley}} \approx 40$ meV resulting from 1% uniaxial strain. Experimentally, a change in valley splitting of < 1 meV can easily be resolved, meaning that the strain can be estimated to a precision of about 0.025%. The largest valley splitting that was observed in this work corresponds to a uniaxial strain of about 0.14%. The average valley splitting observed for seven samples was 1.97 meV, corresponding to an average uniaxial strain of 0.049%. As well as significant sample dependence, the valley splitting also appears to exhibit some spatial dependence, and we discuss this in Supplementary Note 5.

Note that only the $\langle 100 \rangle$ component of strain can be addressed in this work, and this is due to the location of the surface band valleys at the \bar{X} points. The $\langle 110 \rangle$ component of strain would only be observable in a system with valleys located at the \bar{M} points.

An immediate conclusion of the above observation is that residual strain on the order of $\sim 0.1\%$ is probably a ubiquitous feature of STM measurements on cleaved crystals even when deliberate steps are taken to reduce it (see Supplementary Note 1), and it should be considered when using STM to investigate symmetry breaking electronic phenomena. This leads us to caution that this effect could also be significant not only in Landau-quantized systems, but also in intrinsic flatband systems such as the kagomé metals, leading to apparently spontaneous (but actually strain-induced) symmetry breaking in the local density of states.

The observations of valley-selective LL spectra shown in Fig. 4 demonstrate a method of using STM that should be helpful for directly addressing the valley degree of freedom using only a very local r -space measurement covering only a relatively few (~ 100) unit-cells. Although the procedure is used for a square lattice system here, it should also be expected to work straightforwardly for a triangular lattice, and therefore may prove useful for elucidating new valley-related phenomena in a broad range of material systems.

We also introduce a procedure, summarized in Fig. 5, for determining the indices of observed LLs and the Berry phase around a LL orbit in a situation where none of these are initially known. A merit of this technique is that it is agnostic to the underlying band dispersion of the system under investigation. It would have been equally useful if the dispersion had been quadratic, for example, or indeed if it had any arbitrary dispersion. For this reason it is robust against unexpected band distortions due to many-body renormalization effects, and

useful for characterizing them. (We discuss some aspects of the method further in Supplementary Note 6.)

In summary, the above results elucidate how in a multi-valley band structure, a residual strain on a scale of only $\sim 0.1\%$ can lead to extremely valley-polarized LLs, and provide detailed microscopic insights for both strain- and valley-engineering of quantum materials. With a narrower focus on microscopic observations of symmetry breaking states, we also suggest that the strain inferred here is typical of a generic STM measurement, and could impact how measurements of symmetry breaking in other narrow spectroscopic features are interpreted, such as those associated with flatbands or other contributors of van Hove-like signatures.

IV. MATERIALS AND METHODS

A. Crystal synthesis

ZrSiS polycrystals were synthesized by the solid-state reaction using the elemental powders (Zr: 98.8%, Si: 99.99%, and S: 99.995%) with the compositional ratio in evacuated quartz tubes at 1100 °C for 100 hours. Subsequent crystal growth was carried out by the chemical vapor transport method using the polycrystals with 10 wt% of iodine (99.9995%) in evacuated quartz tubes for 100 hours at 1100 °C for the source zone and 1000 °C for the growth zone. The crystal structure, crystal orientation, and chemical composition of the obtained single crystals were evaluated by X-ray diffraction, X-ray Laue back reflection, and X-ray fluorescence techniques, respectively.

B. STM measurements

Crystals were glued using conducting epoxy to either a Cu or Mo sample plate, which was then fixed to a BeCu alloy holder (see Supplementary Note 1). After loading samples into an ultra-high vacuum chamber ($P \sim 10^{-10}$ Torr), surfaces were prepared for STM measurements by cleaving them at about 77 K, before insertion into a modified Unisoku USM1300 low-temperature STM system held at $T = 1.5$ K [42]. STM measurements were performed using electro-chemically etched tungsten tips, which were characterized and conditioned using field ion microscopy followed by repeated mild indentation at a clean Cu(111) surface. Special care was taken to form a tip apex that was both as sharp and as isotropic as possible, which enables effective intra-unit-cell sampling of $\frac{dI}{dV}(V)$ data as described in Fig 4. Tunneling conductance was measured using the lock-in technique with bias modulation of frequency $f_{\text{mod}} = 617.3$ Hz and an amplitude V_{mod} , specified in the caption describing each measurement.

The external magnetic field was applied along the z -axis of the STM system, and for each sample the tilt

of the surface was characterized using STM. It was confirmed that the surface-perpendicular vector was no more than $\sim 1^\circ$ away from the z -axis. This ensures that deviation of the magnetic field strength from the nominal value was negligible.

Conductance maps and their Fourier transforms are plotted using perceptually uniform colormaps [43].

C. DFT calculations

The calculations of the electronic structure of the ZrSiS were performed using a slab construction, using density functional theory (DFT) as implemented in the Vienna *ab initio* simulation package (VASP) [44, 45]. All the calculations were performed using the projector-augmented wave (PAW) [46] pseudopotential with the generalized gradient approximation (GGA) in the form of Perdew-Burke-Ernzerhof (PBE) [47, 48]. The plane-wave cutoff energy was 500 eV and a Γ -centered $4 \times 4 \times 1$ k -mesh was used to describe the electronic structure. The valence orbital set was $4s^2 4p^6 5s^2 4d^2$ for Zr, $3s^2 3p^2$ for Si, and $3s^2 3p^4$ for S. The 7-layer ZrSiS slab with S terminations was modeled utilizing the supercell approach, with the separations between the neighboring slabs being about 21 Å. We used the experimentally obtained lattice parameter $a_0 = 3.544$ Å, as well as the experimental atomic position for the ZrSiS slab [28]. The definition of the strain applied is the discrepancy between lattice constant

a_0 and b_0 (elongating b_0).

ACKNOWLEDGEMENTS

We are grateful to T. Machida and M. Naritsuka for assistance, and to M. Kawamura, P. J. Hsu, T.-M. Chuang and A. Rost for helpful discussions. This work was supported by JST CREST Grant No. JPMJCR16F2 and No. JPMJCR20B4, and also by a Grant-in-Aid for Scientific Research on Innovative Areas ‘Quantum Liquid Crystals’ (KAKENHI Grant No. JP19H05824 and No. JP19H05825), and for ‘Science of 2.5 Dimensional Materials’ (KAKENHI Grant No. JP21H05236), for Scientific Research (A) (KAKENHI Grant No. JP21H04652), and for Challenging Research (Pioneering) (KAKENHI Grant No. JP21K18181) from JSPS of Japan. C.J.B. acknowledges support from RIKEN’s Programs for Junior Scientists. M.-C. J. acknowledges support from RIKEN’s IPA program.

DATA AVAILABILITY

The data that support the findings presented here are available from the corresponding authors upon reasonable request.

-
- [1] E. Fradkin, S. A. Kivelson, M. J. Lawler, J. P. Eisenstein, and A. P. Mackenzie, *Nematic Fermi Fluids in Condensed Matter Physics*. Annu. Rev. Condens. Matter Phys. **1**, 152–178 (2010). <https://doi.org/10.1146/annurev-conmatphys-070909-103925>
- [2] A. Coissard, D. Wander, H. Vignaud, A. G. Grushin, C. Repellin, K. Watanabe, T. Taniguchi, F. Gay, C. B. Winkelmann, H. Courtois, H. Sellier, and B. Sacépé, *Imaging tunable quantum Hall broken-symmetry orders in graphene*. Nature **605**, 51–56 (2022). <https://doi.org/10.1038/s41586-022-04513-7>
- [3] M. J. Lawler, K. Fujita, J. Lee, A. R. Schmidt, Y. Kohsaka, C. K. Kim, H. Eisaki, S. Uchida, J. C. Davis, J. P. Sethna, and E.-A. Kim, *Intra-unit-cell electronic nematicity of the high- T_c copper-oxide pseudogap states*. Nature **466**, 347–351 (2010). <https://doi.org/10.1038/nature09169>
- [4] A. E. Böhrer, J.-H. Chu, S. Lederer, and M. Yi, *Nematicity and nematic fluctuations in iron-based superconductors*. Nature Physics **18**, 1412–1419 (2022). <https://doi.org/10.1038/s41567-022-01833-3>
- [5] B. E. Feldman, M. T. Randeria, A. Gyenis, F. Wu, H. Ji, R. J. Cava, A. H. MacDonald, and A. Yazdani, *Observation of a nematic quantum Hall liquid on the surface of bismuth*. Science **354**, 316–321 (2016). <https://www.science.org/doi/10.1126/science.aag1715>
- [6] C. J. Butler, Y. Kohsaka, Y. Yamakawa, M. S. Bahramy, S. Onari, H. Kontani, T. Hanaguri, and S. Shimoto, *Correlation-driven electronic nematicity in the Dirac semimetal BaNiS₂*. Proc. Natl. Acad. Sci. **119** (49) e2212730119 (2022). <https://doi.org/10.1073/pnas.2212730119>
- [7] C. M. Yim, C. Trainer R. Aluru S. Chi, W. N. Hardy, R. Liang, D. Bonn, and P. Wahl, *Discovery of a strain-stabilised smectic electronic order in LiFeAs*. Nat. Commun. **9**, 2602 (2018). <https://doi.org/10.1038/s41467-018-04909-y>
- [8] Y. Yuan, X. Fan, X. Wang, K. Han, Y. Zhang, Q.-K. Xue, and W. Li, *Incommensurate smectic phase in close proximity to the high- T_c superconductor FeSe/SrTiO₃*. Nat. Commun. **12**, 2196 (2021). <https://doi.org/10.1038/s41467-021-22516-2>
- [9] B. Venkatesan, S.-Y. Guan, J.-T. Chang, S.-B. Chiu, P.-Y. Yang, C.-C. Su, T.-R. Chang, K. Raju, R. Sankar, S. Fongchaiya, M.-W. Chu, C.-S. Chang, G. Chang, H. Lin, A. Del Maestro, Y.-J. Kao, and T.-M. Chuang, *Direct Visualization of Disorder Driven Electronic Liquid Crystal Phases in Dirac Nodal Line Semimetal GdSbTe*. Preprint at <https://doi.org/10.48550/arXiv.2402.18893> (2024).
- [10] E. Fradkin and Steven A. Kivelson, *Liquid-crystal phases of quantum Hall systems*. Phys. Rev. B **59**, 8065 (1999). <https://doi.org/10.1103/PhysRevB.59.8065>
- [11] M. P. Lilly, K. B. Cooper, J. P. Eisenstein, L. N. Pfeiffer, and K. W. West, *Evidence for an Anisotropic State of Two-Dimensional Electrons in High Landau Levels*. Phys.

- Rev. Lett. **82**, 394 (1999). <https://doi.org/10.1103/PhysRevLett.82.394>
- [12] I. Sodemann, Z. Zhu, and L. Fu, *Quantum Hall Ferroelectrics and Nematics in Multivalley Systems*. Phys. Rev. X **7**, 041068 (2017). <https://doi.org/10.1103/PhysRevX.7.041068>
- [13] M. T. Randeria, B. E. Feldman, F. Wu, H. Ding, A. Gyenis, H. Ji, R. J. Cava, A. H. MacDonald, and A. Yazdani, *Ferroelectric quantum Hall phase revealed by visualizing Landau level wavefunction interference*. Nat. Phys. **14**, 796–800 (2018). <https://doi.org/10.1038/s41567-018-0148-2>
- [14] Z. Huang, G. Xian, X. Xiao, X. Han, G. Qian, C. Shen, H. Yang, H. Chen, B. Liu, Z. Wang, and H.-J. Gao, *Tuning Multiple Landau Quantization in Transition-Metal Dichalcogenide with Strain*. Nano Lett. **23**, 8, 3274–3281 (2023). <https://doi.org/10.1021/acs.nanolett.3c00110>
- [15] Y. Xiang, Q. Li, Y. Li, W. Xie, H. Yang, Z. Wang, Y. Yao, and H.-H. Wen, *Twofold symmetry of c-axis resistivity in topological kagome superconductor CsV₃Sb₅ with in-plane rotating magnetic field*. Nat. Commun. **12**, 6727 (2021). <https://doi.org/10.1038/s41467-021-27084-z>
- [16] L. Nie, K. Sun, W. Ma, D. Song, L. Zheng, Z. Liang, P. Wu, F. Yu, J. Li, M. Shan, D. Zhao, S. Li, B. Kang, Z. Wu, Y. Zhou, K. Liu, Z. Xiang, J. Ying, Z. Wang, T. Wu, and X. Chen, *Charge-density-wave-driven electronic nematicity in a kagome superconductor*. Nature **604**, 59–64 (2022). <https://doi.org/10.1038/s41586-022-04493-8>
- [17] Z. Liu, Y. Shi, Q. Jiang, E. W. Rosenberg, J. M. DeStefano, J. Liu, C. Hu, Y. Zhao, Z. Wang, Y. Yao, D. Graf, P. Dai, J. Yang, X. Xu, and J.-H. Chu, *Absence of nematic instability in the kagome metal CsV₃Sb₅*. Preprint at <https://doi.org/10.48550/arXiv.2309.14574> (2023).
- [18] M. Frachet, L. Wang, W. Xia, Y. Guo, M. He, N. Maraytta, R. Heid, A.-A. Haghighirad, M. Merz, C. Meingast, and F. Hardy, *Colossal c-axis response and lack of rotational symmetry breaking within the kagome plane of the CsV₃Sb₅ superconductor*. Preprint at <https://doi.org/10.48550/arXiv.2310.0610> (2023).
- [19] C. Guo, G. Wagner, C. Putzke, D. Chen, K. Wang, L. Zhang, M. Gutierrez-Amigo, I. Errea, M. G. Vergniory, C. Felser, M. H. Fischer, T. Neupert, and P. J. W. Moll, *Correlated order at the tipping point in the kagome metal CsV₃Sb₅*. Nat. Phys. **20**, 579–584 (2024). <https://doi.org/10.1038/s41567-023-02374-z>
- [20] Z. Dai, L. Liu, and Z. Zhang, *Strain Engineering of 2D Materials: Issues and Opportunities at the Interface*. Adv. Mater. **31**, 1805417 (2019). <https://doi.org/10.1002/adma.201805417>
- [21] S. Hosoi, F. Tachibana, M. Sakaguchi, K. Ishida, M. Shimozawa, K. Izawa, Y. Fuseya, Y. Kinoshita, and M. Tokunaga, *Effects of strain-tunable valleys on charge transport in bismuth*. Preprint at <https://doi.org/10.48550/arXiv.2309.05285> (2024).
- [22] L. M. Schoop, M. N. Ali, C. Straßer, A. Topp, A. Varykhalov, D. Marchenko, V. Duppel, S. S. P. Parkin, B. V. Lotsch, and C. R. Ast, *Dirac cone protected by non-symmorphic symmetry and three-dimensional Dirac line node in ZrSiS*. Nat. Commun. **7**, 11696 (2016). <https://doi.org/10.1038/ncomms11696>
- [23] A. Topp, R. Queiroz, A. Grüneis, L. MÜchler, A. W. Rost, A. Varykhalov, D. Marchenko, M. Krivenkov, F. Rodolakis, J. L. McChesney, B. V. Lotsch, L. M. Schoop, and C. R. Ast, *Surface Floating 2D Bands in Layered Nonsymmorphic Semimetals: ZrSiS and Related Compounds*. Phys. Rev. X **7**, 041073 (2017). <https://doi.org/10.1103/PhysRevX.7.041073>
- [24] K. Momma and F. Izumi, *VESTA 3 for three-dimensional visualization of crystal, volumetric and morphology data*. J. Appl. Crystallogr., **44**, 1272–1276 (2011). <https://doi.org/10.1107/S0021889811038970>
- [25] C. J. Butler, Y.-M. Wu, C.-R. Hsing, Y. Tseng, R. Sankar, C.-M. Wei, F.-C. Chou, and M.-T. Lin, *Quasiparticle interference in ZrSiS: Strongly band-selective scattering depending on impurity lattice site*. Phys. Rev. B **96**, 195125 (2017). <https://doi.org/10.1103/PhysRevB.96.195125>
- [26] C.-C. Su, C.-S. Li, T.-C. Wang, S.-Y. Guan, R. Sankar, F. Chou, C.-S. Chang, W.-L. Lee, G.-Y. Guo, and T.-M. Chuang, *Surface termination dependent quasiparticle scattering interference and magneto-transport study on ZrSiS*. New J. Phys. **20**, 103025 (2018). <https://doi.org/10.1088/1367-2630/aae5c8>
- [27] B.-B. Fu, C.-J. Yi, T.-T. Zhang, M. Caputo, J.-Z. Ma, X. Gao, B. Q. Lv, L.-Y. Kong, Y.-B. Huang, P. Richard, M. Shi, V. N. Strocov, C. Fang, H.-M. Weng, Y.-G. Shi, T. Qian, H. Ding, *Dirac nodal surfaces and nodal lines in ZrSiS*. Sci. Adv. **5**, eaau6459 (2019). <https://www.science.org/doi/10.1126/sciadv.aau6459>
- [28] R. Sankar, G. Peramaiyan, I. P. Muthuselvam, C. J. Butler, K. Dimitri, M. Neupane, G. N. Rao, M.-T. Lin, and F. C. Chou, *Crystal growth of Dirac semimetal ZrSiS with high magnetoresistance and mobility*. Sci. Rep. **7**, 40603 (2017). <https://doi.org/10.1038/srep40603>
- [29] M. S. Lodge, E. Marcellina, Z. Zhu, X.-P. Li, D. Kaczorowski, M. S. Fuhrer, S. A. Yang, and B. Weber, *Symmetry-selective quasiparticle scattering and electric field tunability of the ZrSiS surface electronic structure*. Nanotechnology **35**, 195704 (2024). <https://doi.org/10.1088/1361-6528/ad2639>
- [30] Y. Kohsaka, C. Taylor, K. Fujita, A. Schmidt, C. Lupien, T. Hanaguri, M. Azuma, M. Takano, H. Eisaki, H. Takagi, S. Uchida, and J. C. Davis, *An intrinsic bond-centered electronic glass with unidirectional domains in underdoped cuprates*. Science **315**, 1380–1385 (2007). <https://doi.org/10.1126/science.1138584>
- [31] Y. Yen, C.-L. Chiu, P.-H. Lin, R. Sankar, T.-M. Chuang, and G.-Y. Guo, *Dirac nodal line and Rashba spin-split surface states in nonsymmorphic ZrGeTe*. New J. Phys. **23**, 103019 (2021). <https://doi.org/10.1088/1367-2630/ac2b53>
- [32] M. S. Lodge, G. Chang, C.-Y. Huang, B. Singh, J. Hellerstedt, M. T. Edmonds, D. Kaczorowski, M. M. Hosen, M. Neupane, H. Lin, M. S. Fuhrer, B. Weber, and M. Ishigami, *Observation of Effective Pseudospin Scattering in ZrSiS*. Nano Lett. **17**, 7213–7217 (2017). <https://doi.org/10.1021/acs.nanolett.7b02307>
- [33] Q. He, L. Zhou, A. W. Rost, D. Huang, A. Grüneis, L. M. Schoop, and H. Takagi, *Real-space visualization of quasiparticle dephasing near the Planckian limit in the Dirac line node material ZrSiS*. Preprint at <https://doi.org/10.48550/arXiv.2110.11125> (2021).
- [34] L. Jiao, Q. N. Xu, Y. P. Qi, S.-C. Wu, Y. Sun, C. Felser, and S. Wirth, *Observation of Landau quantization and standing waves in HfSiS*. Phys. Rev. B **97**, 195137 (2018). <https://doi.org/10.1103/PhysRevB.97.195137>

- [35] T. Hanaguri, K. Igarashi, M. Kawamura, H. Takagi, and T. Sasagawa, *Momentum-resolved Landau-level spectroscopy of Dirac surface state in Bi_2Se_3* . Phys. Rev. B **82**, 081305R (2010). <https://doi.org/10.1103/PhysRevB.82.081305>
- [36] P. Cheng, C. Song, T. Zhang, Y. Zhang, Y. Wang, J.-F. Jia, J. Wang, Y. Wang, B.-F. Zhu, X. Chen, X. Ma, K. He, L. Wang, X. Dai, Z. Fang, X. Xie, X.-L. Qi, C.-X. Liu, S.-C. Zhang, and Q.-K. Xue, *Landau Quantization of Topological Surface States in Bi_2Se_3* . Phys. Rev. Lett. **105**, 076801 (2010). <https://doi.org/10.1103/PhysRevB.82.081305>
- [37] Y.-S. Fu, M. Kawamura, K. Igarashi, H. Takagi, T. Hanaguri, and T. Sasagawa, *Imaging the two component nature of Dirac–Landau levels in the topological surface state of Bi_2Se_3* . Nat. Phys. **10**, 815–819 (2014). <https://doi.org/10.1038/nphys3084>
- [38] Y.-S. Fu, T. Hanaguri, K. Igarashi, M. Kawamura, M. S. Bahramy, and T. Sasagawa, *Observation of Zeeman effect in topological surface state with distinct material dependence*. Nat. Commun. **7**, 10829 (2016). <https://doi.org/10.1038/ncomms10829>
- [39] W. Zhou, H. Gao, J. Zhang, R. Fang, H. Song, T. Hu, A. Stroppa, L. Li, X. Wang, S. Ruan, and W. Ren, *Lattice dynamics of Dirac node-line semimetal ZrSiS* . Phys. Rev. B **96**, 064103 (2017). <https://doi.org/10.1103/PhysRevB.96.064103>
- [40] P. Dietl, F. Piéchon, and G. Montambaux, *New Magnetic Field Dependence of Landau Levels in a Graphene-like Structure*. Phys. Rev. Lett. **100**, 236405 (2008). <https://doi.org/10.1103/PhysRevLett.100.236405>
- [41] X. Liu, C. Yue, S. V. Erohin, Y. Zhu, A. Joshy, J. Liu, A. M. Sanchez, D. Graf, P. B. Sorokin, Z. Mao, J. Hu, and J. Wei, *Quantum Transport of the 2D Surface State in a Nonsymmorphic Semimetal*. Nano Lett. **21**, 4887–4893 (2021). <https://doi.org/10.1021/acs.nanolett.0c04946>
- [42] T. Hanaguri, *Development of high-field STM and its application to the study on magnetically tuned criticality in $\text{Sr}_3\text{Ru}_2\text{O}_7$* . J. Phys. Conf. Ser. **51**, 514 (2006). <https://doi.org/10.1088/1742-6596/51/1/117>
- [43] K. M. Thyng, C. A. Greene, R. D. Hetland, H. M. Zimmerle, and S. F. DiMarco, *True Colors of Oceanography: Guidelines for Effective and Accurate Colormap Selection*. Oceanography **29**, 9–13 (2016). <https://doi.org/10.5670/oceanog.2016.66>
- [44] G. Kresse and J. Furthmüller, *Efficiency of ab-initio total energy calculations for metals and semiconductors using a plane-wave basis set*. Computational Materials Science **6**, 15–50, (1996). [https://doi.org/10.1016/0927-0256\(96\)00008-0](https://doi.org/10.1016/0927-0256(96)00008-0)
- [45] G. Kresse and J. Furthmüller, *Efficient iterative schemes for ab initio total-energy calculations using a plane-wave basis set*. Phys. Rev. B **54**, 11169 (1996). [10.1103/PhysRevB.54.11169](https://doi.org/10.1103/PhysRevB.54.11169)
- [46] P. E. Blöchl, *Projector augmented-wave method*. Phys. Rev. B **50**, 17953–17979 (1994). [10.1103/PhysRevB.50.17953](https://doi.org/10.1103/PhysRevB.50.17953)
- [47] G. Kresse and D. Joubert, *From ultrasoft pseudopotentials to the projector augmented-wave method*. Phys. Rev. B **59**, 1758 (1999). [10.1103/PhysRevB.59.1758](https://doi.org/10.1103/PhysRevB.59.1758)
- [48] J. P. Perdew, K. Burke, and M. Ernzerhof, *Generalized Gradient Approximation Made Simple*. Phys. Rev. Lett. **77**, 3865–3868 (1996). [10.1103/PhysRevLett.77.3865](https://doi.org/10.1103/PhysRevLett.77.3865)

Supplementary Material for
Valley polarization of Landau levels driven by residual strain
in the ZrSiS surface band

Christopher J. Butler,^{1,*} Masayuki Murase,² Shunki Sawada,²
Ming-Chun Jiang,^{1,3} Daisuke Hashizume,¹ Guang-Yu Guo,^{3,4}
Ryotaro Arita,^{1,5} Tetsuo Hanaguri,^{1,†} and Takao Sasagawa^{2,6}

¹*RIKEN Center for Emergent Matter Science,
2-1 Hirosawa, Wako, Saitama 351-0198, Japan*

²*Laboratory for Materials and Structures,
Tokyo Institute of Technology, Kanagawa 226-8501, Japan*

³*Department of Physics and Center for Theoretical Physics,
National Taiwan University, Taipei 10617, Taiwan*

⁴*Physics Division, National Center for Theoretical Sciences, Taipei 10617, Taiwan*

⁵*Department of Physics, University of Tokyo,
7-3-1 Hongo Bunkyo-ku, Tokyo 113-0033, Japan*

⁶*Research Center for Autonomous Systems Materialogy,
Tokyo Institute of Technology, Kanagawa 226-8501, Japan*

Supplementary Note 1 - Sample nomenclature and efforts to reduce strain

Upon the first observation of an apparent reduced-symmetry electronic state of the kind shown in Fig. 3 of the main text, it needs to be determined whether or not the symmetry breaking is spontaneous. ‘Smoking gun’ evidence for or against the spontaneity of the symmetry breaking might be obtained by observing whether it shows ferroic-like behavior under externally applied strain that is smoothly swept through zero. In principle this could be achieved using recently developed instruments [1], but in absence of this we established the (non-)spontaneity of the symmetry breaking state simply by measuring many samples. Also, instead of deliberately introducing strain, for some samples we took steps to reduce strain caused by differential thermal contraction of the crystal and sample plate.

Short series of magnetic field dependent, valley-selective $dI/dV(V)$ spectra similar to those shown in Fig. 8(a) of the main text were acquired on a total of seven samples. Ordinarily our samples are fixed using epoxy (EpoTek H20E) to thin Cu plates and screwed to BeCu alloy holders using two Mo screws [see Fig. S1(a) and S1(b)]. Anticipating the role of strain we attempted to alter this setup by instead fixing three of the samples to Mo plates and reducing the number of screws from two to one [see Fig. S1(a) and S1(c)]. The choice of Mo as the sample plate results in a better match of the thermal expansion coefficient between ZrSiS and the sample plate, which might reduce strain due to cooling of samples from 300 to 1.5 K [see Fig. S1(d)]. The use of only one screw to secure the Mo sample plate is intended to reduce uniaxial strain due to differing thermal contraction between the sample plate and the BeCu holder.

We identify these various samples with a number that is prefixed by ‘C’ for those mounted on Cu and ‘M’ for those mounted on Mo. Although the origin of residual strain in STM measurements is not well understood, it might be expected that the difference between the two sample setups would lead to some systematic difference in observed valley splitting. However, no such difference was found. Indeed, the sample with the smallest observed valley splitting, and the one with the largest splitting were both mounted on Mo [see Fig. 8(a) of the main text].

* christopher.butler@riken.jp

† hanaguri@riken.jp

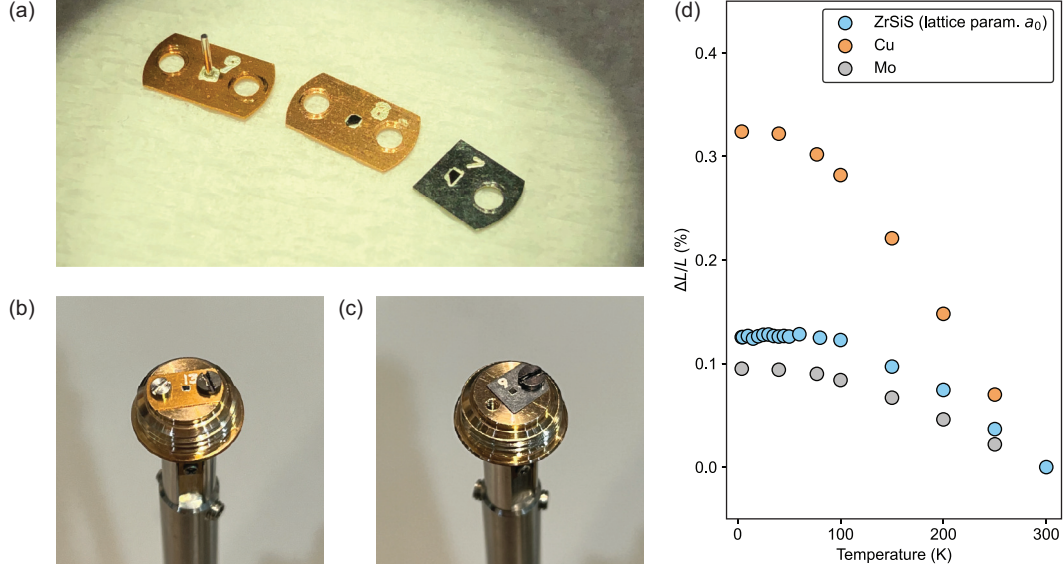


FIG. S1. Efforts to reduce residual strain in cleaved ZrSiS samples. (a) Examples of ZrSiS samples before (left) and after (center and right) cleavage. The samples on the left and in the center are glued to Cu plates, and the sample on the right is glued to a Mo plate. (b) and (c) Sample plates mounted by Mo screws to BeCu alloy sample holders. (c) Measurement of thermal expansion as observed in the lattice parameter a_0 for ZrSiS with varying temperature, as well as values for Cu and Mo [2]. The thermal contraction of ZrSiS is reasonably well matched to that of Mo.

Supplementary Note 2 - Imaging of quasiparticle interference at and between Landau levels

In Fig. S2 we show normalized conductance images $L(\mathbf{r})$ and their Fourier transforms $\mathcal{F}[L(\mathbf{r})]$ for the 26th LL of each valley, as shown in Fig. 3 of the main text. Here we also show the corresponding images extracted at an energy between the 26th and 27th LLs. Because the LLs are formed within the surface bands, between LLs the intensity of the ‘bracket’ signals for surface band scattering appear significantly weaker. Surprisingly, scattering within the bulk bands appears to be absent at the low energies ($|eV| < 10$ meV) where LLs are imaged so that, aside from the atomic corrugation and Bragg peaks, the L and $\mathcal{F}[L]$ images extracted between LLs are almost featureless. This phenomenon of absent bulk band scattering will be discussed in a future report.

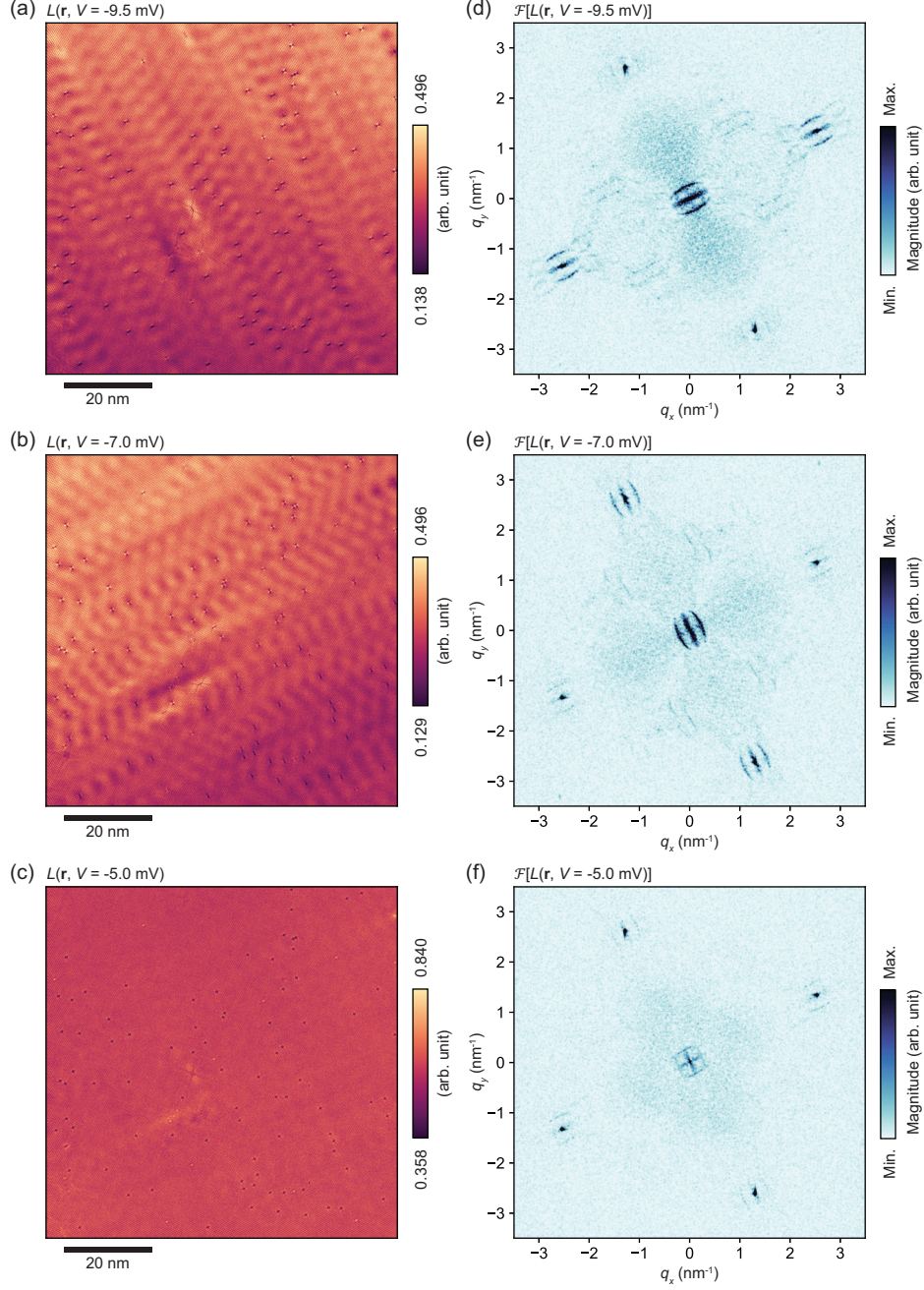


FIG. S2. Conductance imaging at and between valley-polarized LLs. (a) and (b) Normalized conductance images of the 26th LL of each valley, as shown in Fig. 3 of the main text. (c) The normalized conductance image extracted at $V = -5$ mV, in between the 26th and 27th LLs. (d), (e) and (f) The corresponding Fourier transform images. As expected, the intensity of the ‘bracket’ signals for surface band scattering appear significantly weaker between LLs. Surprisingly, the scattering signals associated with the bulk bands are absent for all images.

Supplementary Note 3 - Intra-unit-cell sampling and fitting of dI/dV spectra

Because of the large number of similar measurements in our field dependent series, we process the raw data for each field using a script that automates the following workflow:

- Flatten the simultaneously acquired topography for the given $dI/dV(\mathbf{r}, V)$ measurement and find the reciprocal lattice vectors of the atomic corrugation using 2D Gaussian fitting to the Bragg peaks its Fourier transform.
- Use these reciprocal lattice vectors to generate an r -space lattice of sampling points. The bridge site (and hollow site) lattices are generated by shifting the initial atom-centered lattice by half of the measured lattice constant along either of the lattice vectors (and along both lattice vectors for the hollow sites).
- Sample the $dI/dV(\mathbf{r}, V)$ data at all the points obtained as above, and compute the averaged and valley-disaggregated curves.

This implements the procedure depicted in Fig. 4(f) and 4(g) of the main text, for the data measured at each field. The results for curves acquired at all magnetic fields are shown in Fig S3(b).

Another script is used to perform a fitting procedure to estimate the energies and other properties of the peaks in each curve. The main challenge is that the number of LLs expected to appear in each curve varies, so for each curve a new fitting model with a suitable number of peaks needs to be constructed on-the-fly and without any human intervention. Figure S4 shows how this is achieved.

The model used for fitting is composed of a Gaussian lineshape whose prefactor $A_{\text{back.}}$ is negative, which describes a background on which the LLs lie. The LLs themselves are each described by a Lorentzian lineshape. Accordingly, the conductance curve is modeled as

$$\frac{dI}{dV}(eV) \approx \frac{A_{\text{back.}}}{\sigma_{\text{back.}} \sqrt{2\pi}} \exp \left[-\frac{(eV - E_{\text{back.}})^2}{2\sigma^2} \right] + \sum_i^N \frac{A_i}{\pi} \frac{\Gamma_i/2}{(eV - E_i)^2 + (\Gamma_i/2)^2}. \quad (\text{S1})$$

After some smoothing of the raw $dI/dV(V)$ curves (a 20 point Gaussian convolution – each curve has 401 points), finding the local maxima and minima of a curve gives a first guess

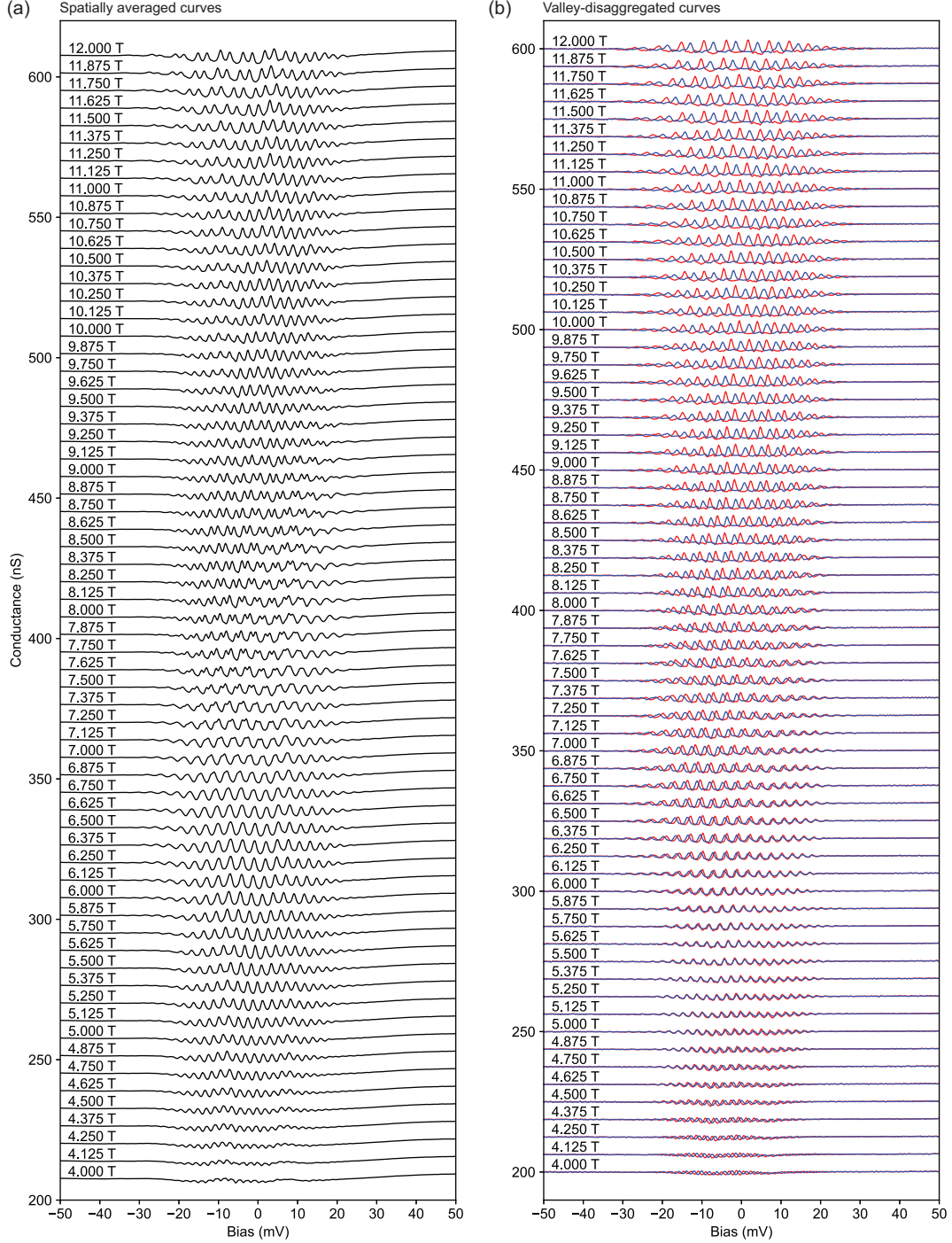


FIG. S3. Valley-disaggregation of $dI/dV(V)$ curves acquired under varying magnetic field. (a) Averages of the measured curves over the $4 \times 4 \text{ nm}^2$ field-of-view shown in Fig. 4 of the main text ($V = 50 \text{ mV}$, $I_{\text{set}} = 500 \text{ pA}$, $V_{\text{mod.}} = 0.25 \text{ mV}$). (b) Valley-selective curves after implementing the intra-unit-cell sampling procedure described for Fig. 4 of the main text.

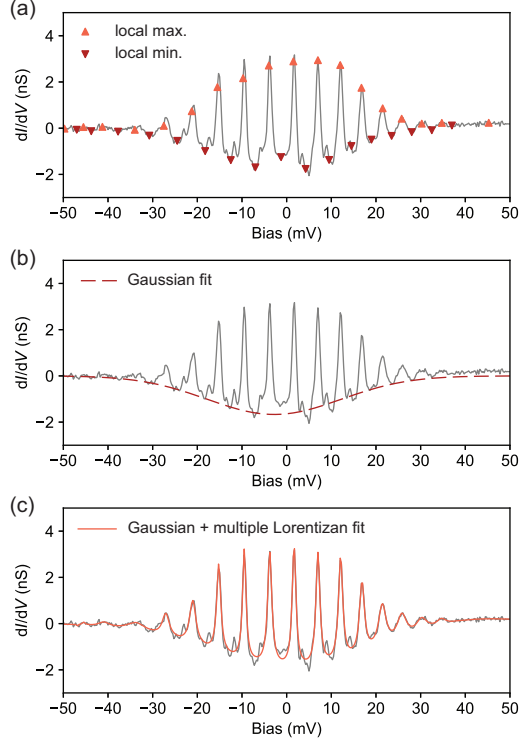


FIG. S4. Fitting procedure for estimating LL energies. (a) One of the valley-selective $dI/dV(V)$ curves obtained using the sublattice sampling method described in Fig. 4 of the main text (specifically, the red curve for $B = 12$ T shown in Fig. S3 above). The local maxima and minima are identified after a 20 point Gaussian smoothing (the curve has 401 points), and these are marked with pink and red triangles, respectively (on top of the *non-smoothed* data). (b) In an intermediate step, a background function is obtained from the set of local minima using fitting with a Gaussian function. (c) Fitting to the non-smoothed data using the full model described by Eq. S8. (The parameters for the Gaussian background are still free parameters of the model.)

at the locations of each of the peaks. In an intermediate step, the Gaussian background is fitted to the local minima, but the parameters for the Gaussian are left as free parameters for the final fitting step. Finally, multiple Lorentzian lineshapes (one for each local maximum) are included to represent peaks in the spectrum. The initial guess of the energy for each peak is informed by the position of a local maximum, and the initial guess for the intensity is informed by the signal value at that location. The initial guess for all peak widths is $\Gamma_{i,\text{ini.}} = 1$ meV.

In practice these peaks include both LLs and noise, and the initial step which picks out

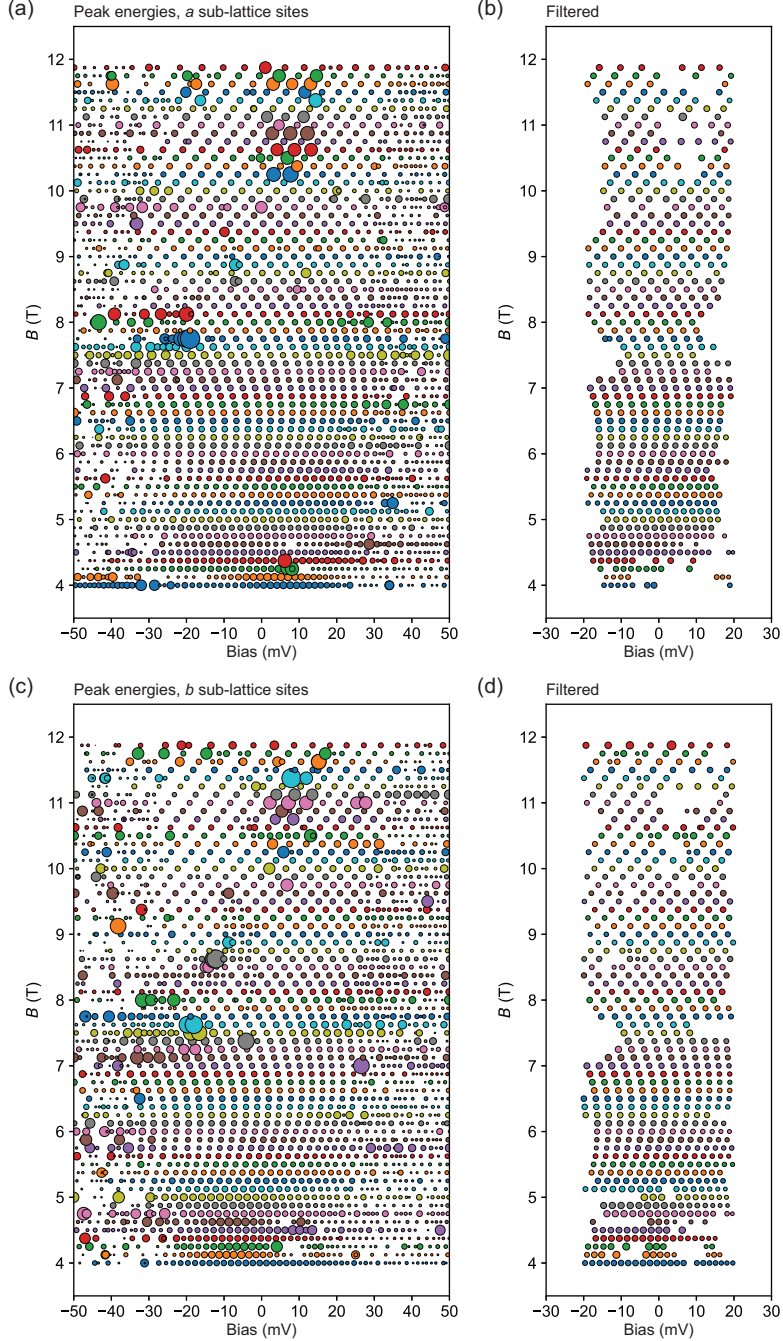


FIG. S5. Filtering of peak fitting results. (a) Energies of peaks found in dI/dV curves sampled at the a sites at all magnetic fields (red curves in Fig. S3). A large number of spurious peaks, for example caused by noise, are found. (b) The remaining points after filtering according to the criteria described in the text. (c) and (d) The corresponding data points obtained from sampling at the b sites (blue curves in Fig. S3).

the local maxima cannot distinguish between them. We proceed with the fitting anyway and use post-fitting filtering of the data points to exclude noise.

We exclude data points that fall outside of a chosen energy interval and those with unphysical features such as a negative intensity or a width smaller than the experimental resolution. We also impose a reasonable cut-off value for the intensity A_i . Thus the filtering criteria are:

- $-20 \text{ meV} < E_i < 20 \text{ meV}$
- $\Gamma_i > 3.5k_B T \approx 0.45 \text{ meV}$
- $0 < A_i < 5 \text{ nS}$

The result is that almost all the remaining peaks correspond to LLs, but many peaks that correspond to LLs are excluded (see Fig. S5) and there is some room for improvement.

Supplementary Note 4 - Landau level peak widths

From the above fitting procedure we obtain not only the LL energies but also their widths, as characterized by the broadening parameter Γ_i of the Lorentzian lineshape fitted

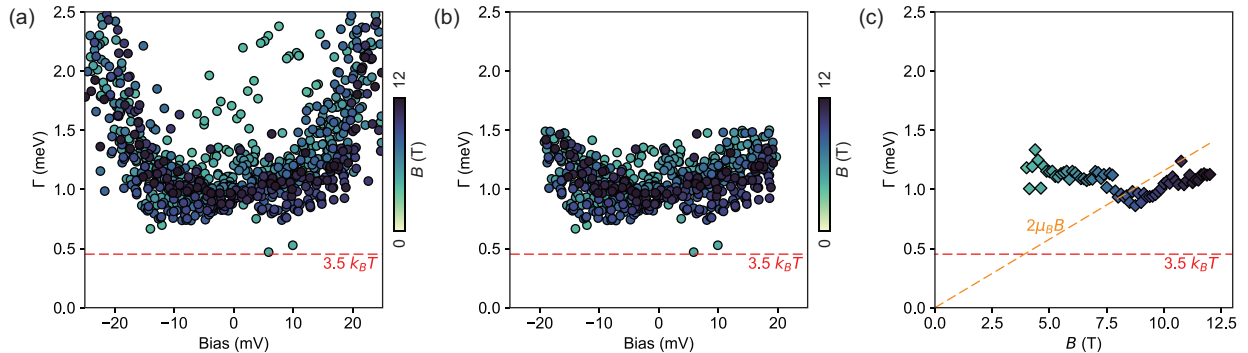


FIG. S6. Landau level peak widths. (a) Peak widths Γ_i , for the peaks found in the curves measured at the a bridge sites and for all magnetic fields. The energy corresponding to the experimental energy resolution, $3.5k_B T$ [3] with $T = 1.5 \text{ K}$, is marked with a pink dashed line. (b) The widths of the peaks remaining after the filtering described for Fig. S5. (c) The average value of the peak widths for each magnetic field. The yellow dashed line gives the Zeeman energy for a free electron as a function of magnetic field.

to each peak. In Fig. S6(a) we show a plot of values Γ_i for the i^{th} peak before filtering out spurious points. Beyond ~ 20 meV from E_F the widths of the peak are seen to abruptly increase, which would be the expected result of a damping effect. However there is only a low confidence that these point actually correspond to LLs. In Fig. S6(b) we show the remaining points after the filtering described above. Here we see that the average width is $\Gamma_i \sim 1$ meV, and there is no strong and consistent relation between the bias voltage and Γ_i . Figure S6(c), which displays the average value of Γ_i with varying magnetic field, shows no systematic field dependence.

In each panel we also show the energy corresponding to our experimental resolution, showing that the apparent width of the LLs is intrinsic and not simply the result of experimental limitations. (Additional measurements performed at $T = 0.35$ K confirm this.) The intrinsic width of the Landau levels is attributable to quasiparticle scattering. Invoking the energy-time uncertainty relation $\Delta E \cdot \Delta t = \Gamma \cdot \tau \geq \hbar/2$, the width corresponds to a timescale of $\tau = 6.58 \times 10^{-13}$ s. Given the measured average velocity of the surface band, $\tilde{v} \approx 4.5 \times 10^5$ m/s, this would correspond to a quasiparticle mean free path of about 150 nm. Another way to characterize the scattering rate for a Landau level is as a Dingle temperature $T_D = \hbar / (2\pi k_B \tau) \approx 1.85$ K [4].

Supplementary Note 5 - Spatial mapping of strain

As well as significant sample dependence, the valley splitting also shows some spatial variation. In the measurements shown for sample C8 in the main text, this can be characterized by the variation in the energy difference between the two valley-polarized sub-levels visualized in Fig. 3. The $dI/dV(\mathbf{r}, V)$ measurement from which the images in Fig. 3 are derived spans the energy range from -10.5 to -4.5 meV, covering two peaks. We fit a function to these peaks consisting of a pair of Lorentzian lineshapes on a linear background:

$$\begin{aligned} \frac{dI}{dV}(eV) \approx & \frac{A_a}{\pi} \frac{\Gamma_a/2}{(eV - E_a)^2 + (\Gamma_a/2)^2} \\ & + \frac{A_b}{\pi} \frac{\Gamma_b/2}{(eV - E_b)^2 + (\Gamma_b/2)^2} \\ & + m(eV) + c \end{aligned} \quad (\text{S2})$$

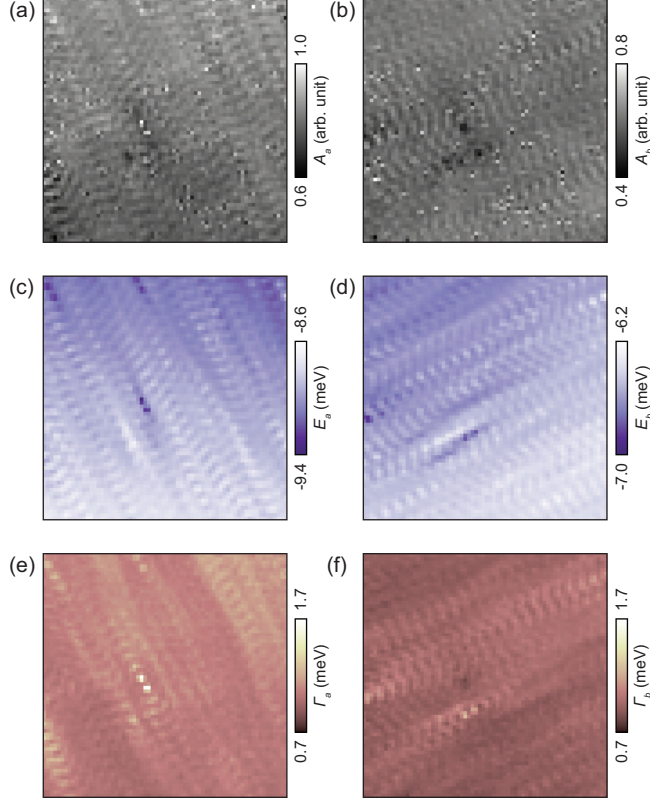


FIG. S7. Results of fitting a pair of Lorentzian functions to the pair of LL peaks in the $dI/dV(\mathbf{r}, V)$ data underpinning Fig. 3 of the main text. Fitting is performed at each pixel after a 10×10 pixel course-graining of the raw data. (a) Intensities A_a and A_b . (b) Energies E_a and E_b . (c) Peak widths Γ_a and Γ_b .

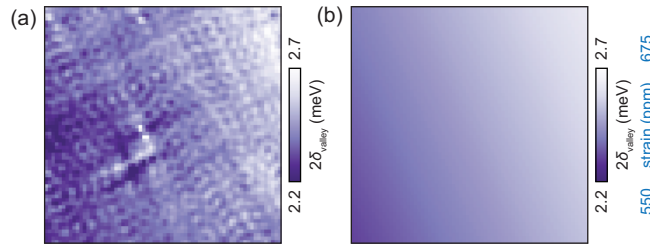


FIG. S8. Spatial imaging of $2\delta_{\text{valley}}$. (a) An image of $E_b - E_a = 2\delta_{\text{valley}}$. (b) A planar fit to the image in (a). The equivalent range of values for strain are shown alongside the colorbar.

Figure S7 shows the resulting optimized fitting parameters for $A_{a(b)}$, $E_{a(b)}$ and $\Gamma_{a(b)}$. We then obtain $E_b - E_a = 2\delta_{\text{valley}}$, which is plotted in Fig. S8(a). Although the map of $2\delta_{\text{valley}}$ shows spatial modulations that resemble the quasiparticle interference modulations in Fig. 3 of the main text, these are probably a spurious artifact of the fitting procedure. The

global trend, clarified by the planar fit shown in Fig. S8(b), is a finite variation of $2\delta_{\text{valley}}$ over larger length scales. The corresponding values for local strain, that we estimate using arguments given in the main text, are also shown. The field of view is $80 \times 80 \text{ nm}^2$, and we see a variation of 125 ppm over a 100 nm length scale. Extrapolating this variation out to a scale approaching the size of the sample ($\sim 1 \text{ mm}$) quickly results in unfeasibly large strain. The actual distribution must have significant inhomogeneities, e.g. ripples or wrinkles, on scales larger than the field-of-view shown here, but much smaller than the sample size.

Supplementary Note 6 - Considerations for LL indices & Berry phase search procedure

To determine the LL indices and Berry phase around the surface band contours, we use a process of minimizing the spread, characterized as σ , of the LL energy points in a E -versus- νB plot (see Fig. 5 of the main text). Here we investigate how the effectiveness of this process varies as fewer data points are used, representing a shorter measurement. First, we select the subset for $B \leq 9 \text{ T}$ (for a more economical superconducting magnet configuration, solid blue curve in Fig. S9). We also try subsets of the data at increasingly sparse values of magnetic field strength. Instead of using an increment of $\Delta B = 0.125 \text{ T}$, as shown in the main text, we take only the subset of data at increments of $\Delta B = 0.25 \text{ T}$, 0.5 T , and 1 T

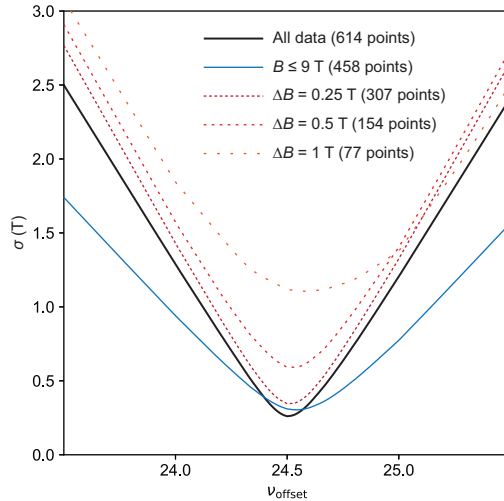


FIG. S9. Minimization of the spread, σ , of LL energy data points in E -versus- νB space, using only various subsets of the total data set.

(dashed curves in Fig. S9). In all cases σ is minimized closer to $\nu_{\text{offset}} = 24.5$ than to 24 or 25, in agreement with the result shown in the main text and indicating a Berry phase of $\gamma_B = 0$. The result is fairly convincing if an increment of $\Delta B \leq 0.5$ T is used, with 154 data points remaining, but appears less reliable for greater increments and fewer points.

Given that an increment of $\Delta B = 0.5$ T would lead to a decisive result, the challenge would then be the assignment of provisional indices $\nu_{\text{prov.}}$. This is because if $\nu_{\text{prov.}}$ is assigned by hand, it is difficult to track which peaks in different conductance curves belong to the same LL if the change in field causes the LL energy to change by more than a fraction of the energy interval between two LLs. We leave this as an issue to be addressed in the future.

From Eqn. 4 of the main text, while σ is the average contribution to the spread of the data points in a E -versus- νB plot, σN is the total spread. The minimum possible value for σN is the span of the points along the νB axis, but this simply corresponds to the span along the E axis where LLs can be observed [see Fig. 5(b) of the main text as an example], which depends on such details as the width of the band hosting LLs and, as we speculate in the main text, attenuation of the LL peaks due to e - ph interactions.

-
- [1] C. W. Hicks, M. E. Barber, S. D. Edkins, D. O. Brodsky, A. P. Mackenzie, *Piezoelectric-based apparatus for strain tuning*. Rev. Sci. Instrum. **85**, 065003 (2014). <https://doi.org/10.1063/1.4881611>
 - [2] J. W. Ekin, *Experimental Techniques for Low-temperature Measurements*. (Oxford University Press, Oxford 2011).
 - [3] C. J. Chen, *Introduction to Scanning Tunneling Microscopy*. (Oxford University Press, Oxford, 2008).
 - [4] R. B. Dingle, *Some magnetic properties of metals II. The influence of collisions on the magnetic behaviour of large systems*. Proc. R. Soc. Lond. A Math. Phys. Sci. **211**, 517–525 (1952). <https://doi.org/10.1098/rspa.1952.0056>